ELSEVIER

Journal of African Earth Sciences 37 (2003) 161–190

Journal of African Earth Sciences

www.elsevier.com/locate/jafrearsci

The LATEA metacraton (Central Hoggar, Tuareg shield, Algeria): behaviour of an old passive margin during the Pan-African orogeny

Jean Paul Liégeois [a,*], Louis Latouche [b,✠], Mustapha Boughrara [b], Jacques Navez [a], Michel Guiraud [b]

[a] *Isotope Geology, Africa Museum, B-3080 Tervuren, Belgium*

[b] *Laboratoire de Minéralogie, FRE. 2456 CNRS, Muséum National d'Histoire Naturelle, 61 rue Buffon, F-75005 Paris, France*

Received 13 July 2002; accepted 7 May 2003

Abstract

Historically, the Tuareg shield is divided into three parts bordered by mega-shear zones with the centre, the Central Polycyclic Hoggar, characterized by Archaean and Palaeoproterozoic lithologies. Nearly 10 years ago, the Tuareg shield was shown to be composed of 23 displaced terranes [Geology 22 (1994) 641] whose relationships were deciphered in Aïr to the SE [Precambr. Res. 67 (1994) 59]. The Polycyclic Central Hoggar terranes were characterized by the presence of well preserved Archaean/Palaeoproterozoic and Neoproterozoic lithologies.

We show here that the terranes from Central Hoggar (Laouni, Azrou-n-Fad, Tefedest, Egéré-Aleksod) belonged to a single old passive margin, to which we gave the acronym name LATEA, which behaved as a craton during the Mesoproterozoic and the Early-Middle Neoproterozoic but was partly destabilized and dissected during the Late Neoproterozoic as a consequence of its involvement as a passive margin in the Pan-African orogen.

An early Pan-African phase consisted of thrust sheets including garnet-bearing lithologies (eclogite, amphibolite, gneiss) that can be mapped and correlated in three LATEA terranes. In the Tin Begane area, *P–T–t* paths have been established from >15 kbar—790 °C (eclogite) to 4 kbar—500 °C (greenschist retrogression) through 12 kbar—830 °C (garnet amphibolite) and 8 kbar—700 °C (garnet gneiss), corresponding to the retrograde path of a Franciscan-type loop. Sm–Nd geochronology on minerals and laser ablation ICP-MS on garnet show the mobility of REE, particularly LREE, during the retrograde greenschist facies that affects, although slightly, some of these rocks. The amphibolite-facies metamorphism has been dated at 685 ± 19 Ma and the greenschist facies at 522 ± 27 Ma. During the thrust phase, the Archaean–Palaeoproterozoic basement was only locally affected by the Pan-African tectonics. LATEA behaved as a craton. Other juvenile terranes were also thrust early onto LATEA: the Iskel island arc at ≈850 Ma to the west of LATEA, the Serouenout terrane in the 700–620 Ma age range to the east. No subduction-related magmas have intruded LATEA during this epoch, which behaved as a passive margin.

During the main Pan-African phase (625–580 Ma), LATEA was dissected by mega-shear zones that induced several hundreds km of relative displacement and allowed the emplacement of high-K calc-alkaline batholiths. Smaller movements continued till 525 Ma, accompanied by the emplacement of subcircular plutons with alkaline affinity. Here is dated the Ounane granodiorite (624 ± 15 Ma; $^{87}Sr/^{86}Sr_i = 0.70839 \pm 0.00016$; 6WR, MSWD = 0.87) and the Tisselliline granite (552 ± 15 Ma; $^{87}Sr/^{86}Sr_i = 0.7074 \pm 0.0001$; 5WR, MSWD = 1.4). Nd isotopes indicate a preponderant Palaeoproterozoic crustal source for these two plutons: $\varepsilon_{Nd} = -14$ to -21 at 624 Ma and T_{DM} = 1650–2320 Ma for Ounane and $\varepsilon_{Nd} = -13$ to -15 at 555 Ma and T_{DM} = 1550–1720 Ma for Tisselliline. Our model links these intrusions to a linear lithospheric delamination along mega-shear zones, allowing the hot asthenosphere to rise, melt by adiabatic pressure release and inducing the melting of the Palaeoproterozoic and Archaean lower crust.

* Corresponding author. Tel./fax: +32-2-6502252.

E-mail addresses: jean-paul.liegeois@africamuseum.be (J.P. Liégeois), jacques.navez@africamuseum.be (J. Navez), guiraud@mnhn.fr (M. Guiraud).

✠ Deceased, June 2003.

0899-5362/$ - see front matter
doi:10.1016/j.jafrearsci.2003.05.004

The LATEA cratonic microcontinent remained however sufficiently rigid to preserve Archaean and Palaeoproterozoic lithologies as well as Middle Neoproterozoic oceanic thrust sheets. This corresponds to the notion of metacraton [J. African Earth Sci. 34 (2002) 119], i.e. a craton that has been remobilized during an orogenic event but is still recognizable dominantly through its rheological, geochronological, isotopic and sometimes petrological characteristics.

Keywords: Metacraton; High-K calc-alkaline batholith; Pan-African; Hoggar; Tuareg shield

1. Introduction

The Tuareg shield was mainly built during the Pan-African orogeny at 600 ± 30 Ma. In addition, magmatic rocks are known between 870 and 520 Ma, corresponding to early accretion events and final post-collisional events. The Tuareg shield presents the whole width of an orogen from the West African craton to the west, to the Saharan metacraton to the east. Juvenile Neoproterozoic oceanic and Archaean–Palaeoproterozoic (≈2 Ga) lithologies range from well preserved to completely remobilized ones. Historically, the Suggarian (= high-grade metamorphic rocks) was separated from the Pharusian (= low-grade metamorphic rocks) (Kilian, 1932; Lelubre, 1952). The Western Hoggar, dominated by low-grade upper Proterozoic sedimentary and volcanic rocks was called the "Pharusian belt" although containing a granulitic block (In Ouzzal; Fig. 1A and B). The Central Hoggar, presenting Archaean and Palaeoproterozoic high-grade basement rocks reactivated to varying degrees by the Pan-African orogeny and including some "Pharusian basins" was called the "Polycyclic Central Hoggar". To the east, basements considered as pre-Neoproterozoic were grouped together with the narrow linear intracontinental Tiririne belt in an "Eastern Hoggar" (Fig. 1A; Bertrand and Caby, 1978; Bertrand et al., 1978). N–S mega-shear zones separate these three provinces and the correlations between them were restricted to metamorphic grade and to geochronology. In the Central Hoggar, the basal layers of the so-called "Pharusian basins" are mylonites (Latouche, 1985; Bertrand et al., 1986).

Nearly 10 years ago, Black et al. (1994) showed that the Tuareg shield was made of 23 displaced terranes (Fig. 1B) with their own lithological, metamorphic, magmatic and tectonic characteristics, being separated by subvertical strike-slip shear zones or by major thrust fronts. A model for relationships between the terranes was proposed for the SE Tuareg shield in Aïr (Liégeois et al., 1994) while other terranes appear to be exotic such as the Iskel terrane (Fig. 2) built at 870–850 Ma (Caby et al., 1982) to the east of the Pharusian belt or as the Tchilit terrane in Aïr with ≈2 Ga bimodal volcanic rocks (Navez et al., 1999).

In this work, we address the evolution of the Central Hoggar during Neoproterozoic times. We propose a model of metacraton (= partly destabilized craton; Abdelsalam et al., 2002) integrating data in the literature and new data presented here. We use a multidisciplinary approach including field, structural, petrological, geochemical, geochronological and geophysical data. The relationships with the other parts of the Tuareg shield are also proposed.

2. Geological setting

The Central Hoggar is made of four terranes: Laouni, Azrou-n-Fad, Tefedest, Egéré-Aleksod (Figs. 1B and 2) that are grouped here under the acronym "LATEA" since, as we will see, they share fundamental features. LATEA is bounded to the East by the mainly juvenile Serouenout terrane and to the west by the ≈850 Ma Iskel terrane (Fig. 2). These four LATEA terranes are made of a Palaeoproterozoic basement (Bertrand et al., 1986) with Archaean lithologies to the north of Egéré-Aleksod (Latouche and Vidal, 1974; Peucat et al., 2003, this issue). On less than 10% of the surface of these four terranes, low-grade Neoproterozoic rocks are bounded by tectonic contacts (Bertrand and Caby, 1978). Neoproterozoic granitoids are abundant particularly to the south and to the west.

Two areas in LATEA (Fig. 2) are the focus of this study, the first in the south, the Tin Begane area (Fig. 3), and the second to the north, the Gour Oumelalen area (Fig. 4).

2.1. The Tin Begane area

The Tin Begane area belongs to the Laouni terrane and is characterized by mega-thrusts (Figs. 2 and 3). The southernmost thrust, 100 km long and NW–SE oriented, is marked by serpentinites, peridotites, mafic–ultramafic rocks, black shales, garnet micaschists and Mn-rich pods, interpreted as ophiolitic remnants (Tessalit Mountains; Black et al., 1994; Fig. 2). To the south and all along this structure, ultramafic–mafic layered intrusions of lithospheric mantle origin intruded during the post-collisional period (Cottin et al., 1998). This attests that the thrust is rooted in a lithospheric structure, likely to be an early suture. In the middle of this composite terrane, a 100 km long mega-thrust is underlined by a nearly continuous eclogitic level (Figs. 2 and 3). The latter constitutes a key structure and lithology: it can be

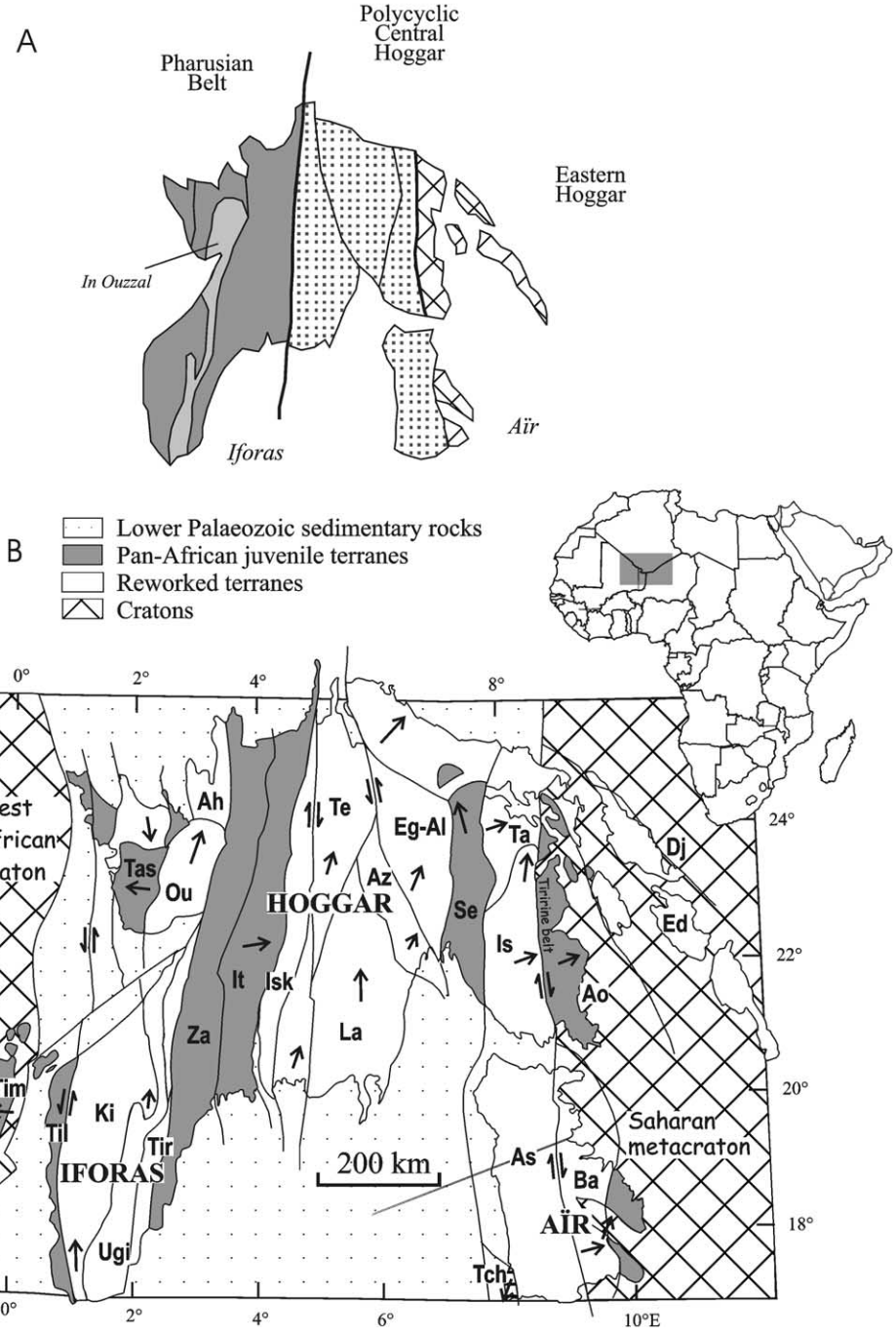

Fig. 1. Tuareg shield: (A) first subdivision (Bertrand and Caby, 1978); (B) Tuareg shield terrane map (from Black et al., 1994). Solid arrow = movement direction. From east to west, 23 terranes are Djanet (Dj), Edembo (Ed), Aouzegueur (Ao), Barghot (Ba), Assodé-Issalane (As-Is), Tchilit (Tch), Tazat (Ta), Serouenout (Se), Egéré-Aleksod (Eg-Al), Azrou-n-Fad (Az), Tefedest (Te), Laouni (La), Iskel (Isk), In Teidini (It), Tin Zaouatene (Za), Tirek (Tir), Ahnet (Ah), In Ouzzal (Ou), Iforas granulitic unit (Ugi), Tassendjanet (Tas), Kidal (Ki), Tilemsi (Til), Timétrine (Tim).

followed from the south to the north of the shield, in the Azrou-n-Fad terrane, to the south (Sautter, 1986) and to the north (Latouche, 1985) of the Egéré-Aleksod terrane (Fig. 2). In all these structures, stretching lineations are oriented ≈N30°E and shear sense criteria (rotated porphyroblasts, shape fabric of quartz grains, preferred orientation of quartz C axes, mica elongated aggregates, C–S structures) indicate a general NNE movement (Bertrand et al., 1986).

To the north of the eclogites, the Laouni terrane is characterized by large basin and dome structures comprising orthogneisses, amphibolites and paragneiss. The

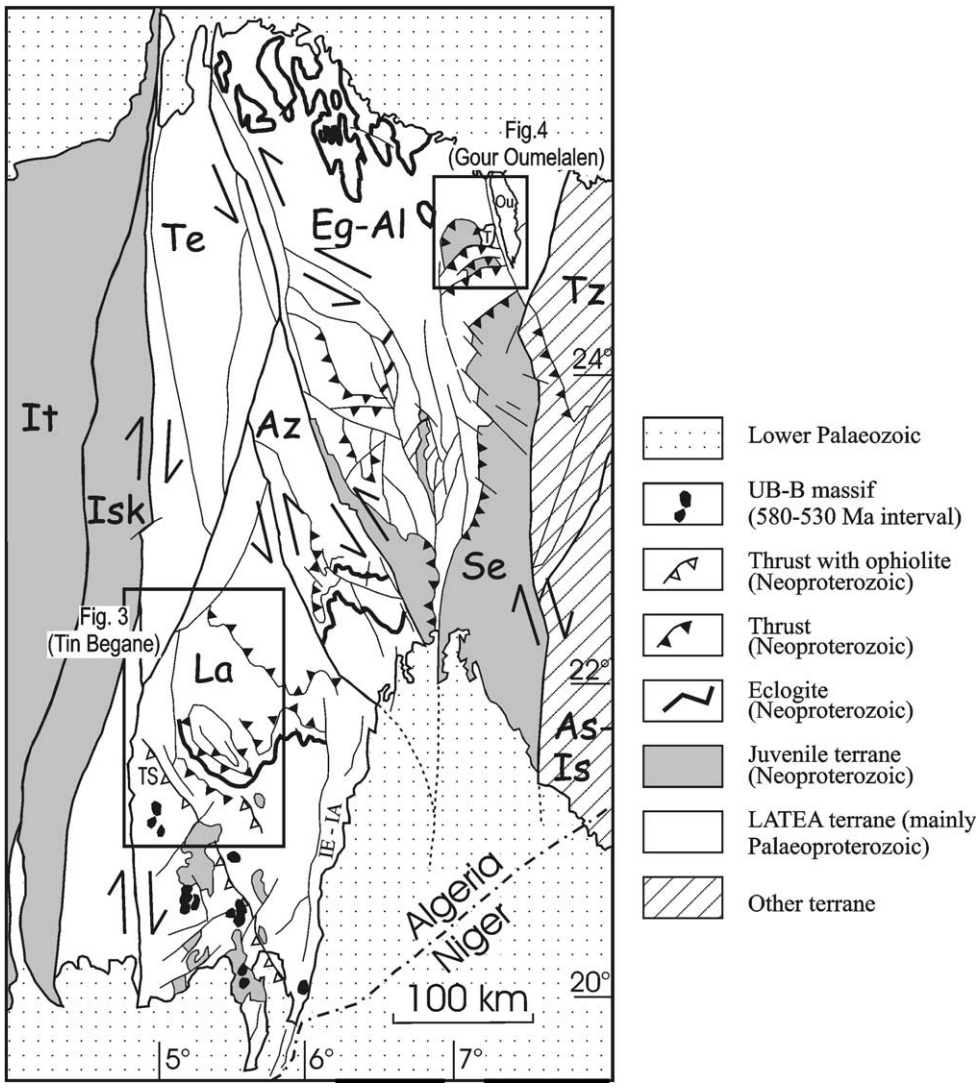

Fig. 2. Sketch map of terranes from the Central Hoggar. Eg-Al = Egéré-Aleksod, Te = Tefedest, Az = Azrou-n-Fad, Se = Serouenout, Is = Issalane, La = Laouni, Isk = Iskel, It = In Teidini. Figs. 3 (Tin Begane) and 4 (Gour Oumelalen) areas are represented. TS = Tessalit mountains; Ou = Ounane; T = Tisselliline; IE-IA = In Ebbeggui–In Attei domain.

regional structure corresponds to stretching of imbricate thrust sheets upon reactivated Eburnian (≈2 Ga) granulites known as remnants at all scales and upon subcontemporaneous garnet-cordierite migmatitic granite. Mixed U–Pb zircon Concordia age on granulites and migmatitic granite gave an Eburnian age of 2069 ± 49 Ma (Iherane area on Fig. 3; Bertrand et al., 1986, recalculated following Ludwig, 1999). Recalculated ages on individual lithologies give 1979 ± 33 Ma with a lower intercept of 209 ± 150 Ma for the granulites and 2038 ± 15 Ma with a lower intercept of 130 ± 170 for the migmatitic granite, the zircon fractions being close to the upper intercept in both cases. These results indicate the absence of Neoproterozoic effect on these zircons and demonstrate the Eburnian age of the granulitic metamorphism. In some places, the discordance of zircon fractions may be higher as for the Telohat migmatite (north of Azrou-n-Fad terrane, Fig. 1; Barbey et al., 1989: upper intercept: 2131 ± 12 Ma, lower intercept: 609 ± 17 Ma with $t_{207/235}$ between 1450 and 1635 Ma), which renders the interpretation of the age of the migmatitization more ambiguous.

Pan-African syn-kinematic granites intruded in the range 620–580 Ma and generally present a subhorizontal foliation (e.g. the Anfeg (608 ± 7 Ma) and Tinef (604 + 11/−8 Ma) batholiths [recalculated following Ludwig, 1999], U–Pb zircon, with concordant titanite at 580 Ma for Tin Amzi pluton; Bertrand et al., 1986; Fig. 3). Their emplacement is related to movements along subvertical shear zones associated with secondary subhorizontal structures (Acef et al., 2003, this issue). To the south of the eclogites, the Laouni terrane is mainly made of granitoid plutons (>70% of the surface). The ophiolitic remnant lies in that area. To the east of the

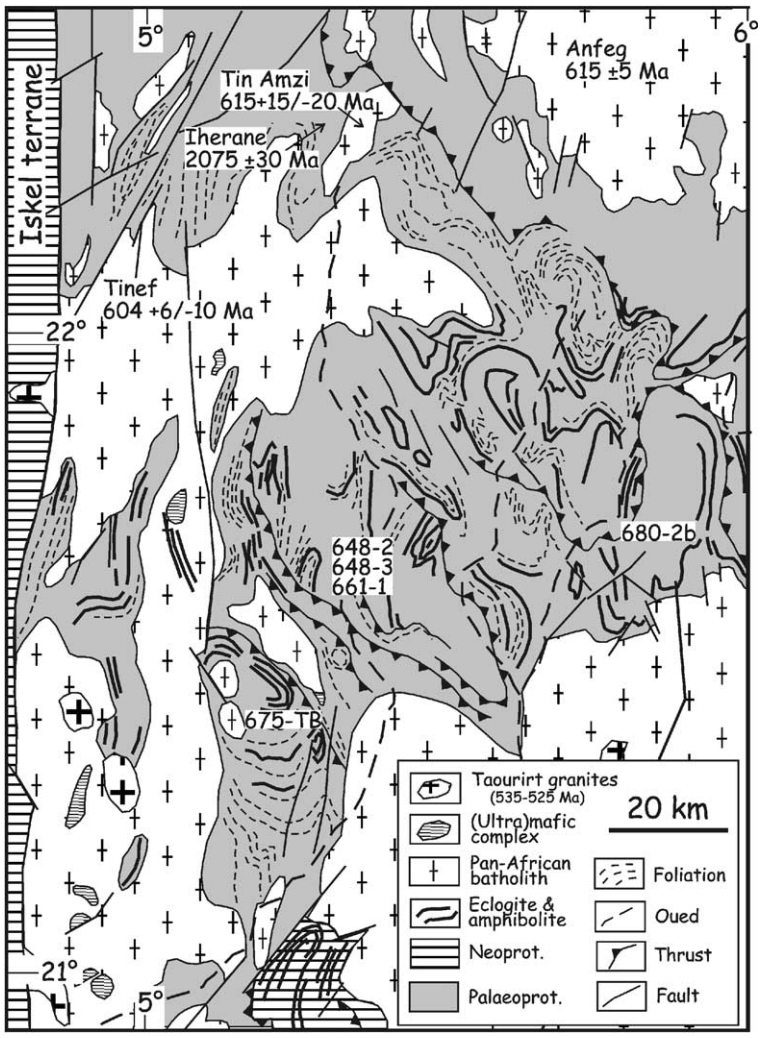

Fig. 3. Structural sketch map of the Tin Begane area. Localization of the samples used for Sm–Nd geochronology. The ages on the map are U–Pb on zircon data from Bertrand et al. (1986). The age range mentioned for the Taourirt granites are from Cheilletz et al. (1992) and Paquette et al. (1998). The ultramafic–mafic complexes are in the range 580–525 Ma (Cottin et al., 1998). The eclogites and the amphibolites are Neoproterozoic (this study).

terrane, lithologies comprising very fine-grained felsic rocks, mylonitic amphibole gneisses, thin layers of quartzite and pyroxenite (In Ebeggui–In Attei domain; Fig. 2) are in sharp contact with the main part of the Laouni terrane through a N–S shear zone cross-cutting the eclogitic horizon. This area is reminiscent of the Palaeoproterozoic Tchilit terrane in the SE Tuareg shield (Aïr; Navez et al., 1999; Fig. 1).

Four main Pan-African tectono-metamorphic phases are known in the Laouni terrane: (1) ductile thrusts associated to eclogites; (2) flat mylonitic thrusts with abundant sheath folds and mineral stretching lineations indicating transport to the NE. These thrusts reworked the preceding structures, generating a tectonic melange including Palaeoproterozoic basement lithologies and juvenile Neoproterozoic material. This phase occurred in the amphibolite facies; (3) during the syn-kinematic granitoid emplacement (610–580 Ma; Bertrand et al., 1986), basin and dome structures contemporaneous with large movements along subvertical mega-shear zones, HT-LP metamorphism and lithospheric thinning (Cottin et al., 1990; Guiraud et al., 1996) accompanied by late troctolitic-noritic layered intrusions (Cottin et al., 1998); and (4) the last event corresponds to faulting along pre-existing shear zones that accompanied the intrusion of shallow-depth peraluminous Sn–W leucogranites at 535–525 Ma (Ar–Ar; Cheilletz et al., 1992). This last age corresponds to the cessation of the movement along the main shear zones located to the west of LATEA as outlined by the Tioueine pluton (523 ± 1 Ma; Paquette et al., 1998) within the Iskel terrane. In the Laouni terrane, ages between 580 and 540 Ma have not been measured although such ages are known elsewhere in the Tuareg shield such as in the Kidal terrane in the Iforas region (Liégeois et al., 1987, 1996; Fig. 1).

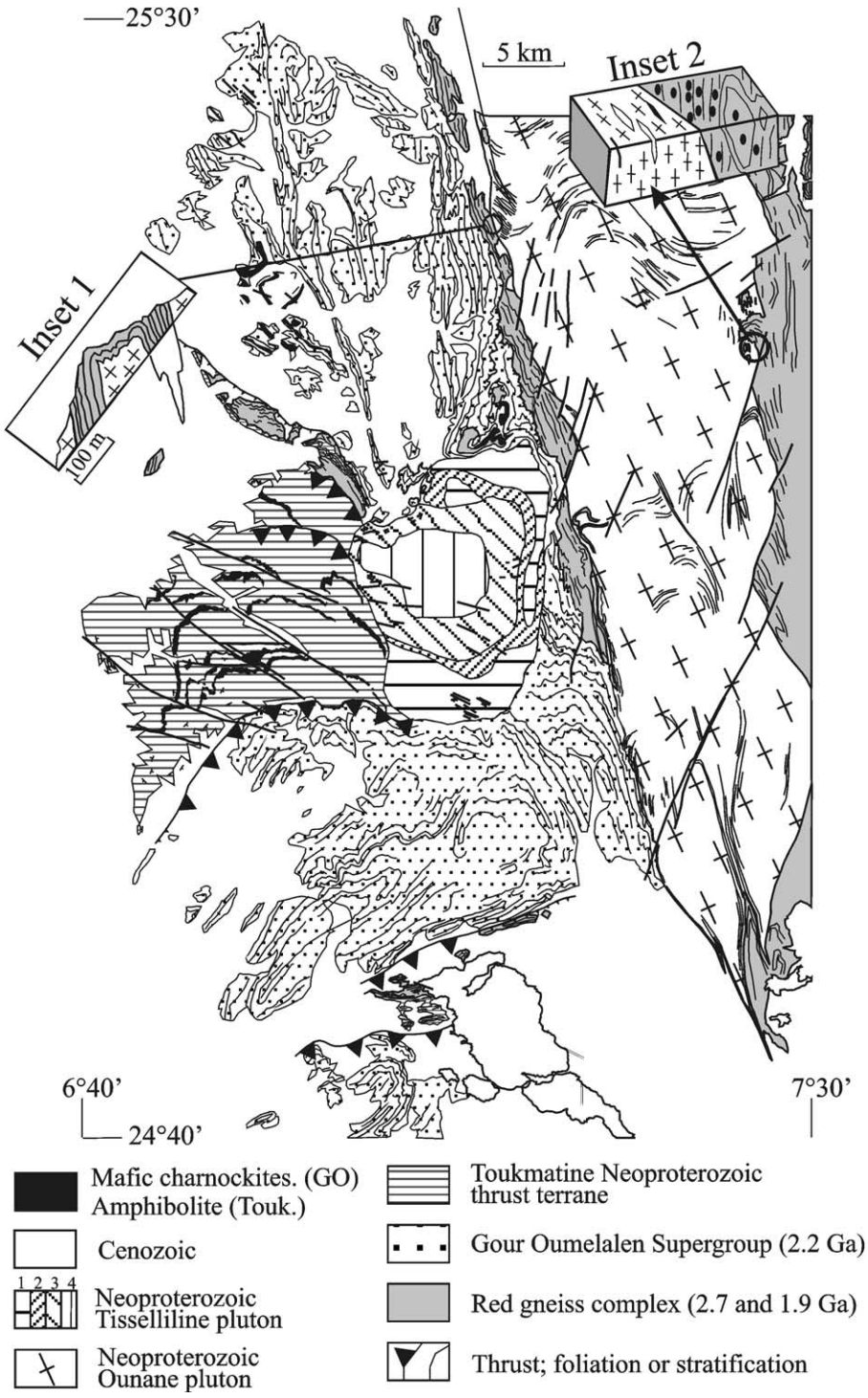

Fig. 4. Gour Oumelalen geological map. From Latouche (1978) with unpublished data from Boissonnas for the Tisselliline pluton (1 = coarse-grained granite; 2 = "black" granite; 3 = medium-grained granite; 4 = fine-grained granite). Insets 1 and 2 represent cross-sections whose location is indicated by the origin of the arrow. GO = Gour Oumelalen; Touk. = Toukmatine; Mafic charnockites = Mafic facies from the charnockitic series. Ages for gneisses are from Peucat et al. (2003, this issue).

2.2. The Gour Oumelalen area

2.2.1. The Archaean and Palaeoproterozoic basement

The Gour Oumelalen area, located along the north-eastern boundary of the Egéré-Aleksod terrane (Fig. 2), is one of the best-preserved Archaean and Palaeoproterozoic zones in Central Hoggar. It is mainly composed of granulites (Latouche, 1978; Pineau et al., 1976). Three units were defined by Latouche (1978, 1983; Fig. 4). The Red Gneiss Complex (1) is composed of two types of

gneiss (Peucat et al., 2003, this issue): the first group is dated (U–Pb on zircon) at ≈2650–2700 Ma with T_{DM} Nd model ages in the 3100–3200 Ma range and the second group has an age of ≈1900 Ma, with younger Nd model ages, although still Archaean, for their protoliths (T_{DM} model ages between 2500 and 2800 Ma). The Red gneiss complex is well-represented within the shear zone bordering the western flank of the Ounane pluton (Fig. 4), but elsewhere it is tectonically overlain by the Gour Oumelalen Supergroup (2), consisting of a granulitic metasedimentary sequence deposited between 2400 and 1900 Ma (Peucat et al., 2003, this issue). They were both intruded by mafic and felsic charnockites at ≈1900 Ma (Peucat et al., 2003, this issue). The younger unit is the Toukmatine Group (3) of Neoproterozoic age, which corresponds to Pan-African nappes and slivers of supracrustal metapelitic schists and meta-ophiolites, thrust towards the north on the Gour Oumelalen area from the Serouenout terrane (Figs. 2 and 4). This situation is similar to the juvenile thrust sheets in the Tin Begane area, although the difference in thrust direction suggests they correspond to distinct events with different ages. In addition, Neoproterozoic granitoids intruded both the Archaean–Palaeoproterozoic basement and the thrust Neoproterozoic juvenile series, mainly along mega-shear zones (Ounane and Tisselliline plutons; Fig. 4).

2.2.2. The Neoproterozoic Ounane and Tisselliline plutons

Two different Neoproterozoic plutons were studied. The first (Ounane) is elongated within the general orientation of the Pan-African shear zone while the second (Tisselliline) presents a circular shape but is moulded on the structures, particularly on its eastern flank, linked to the transpressive shear tectonics (Fig. 4).

The Ounane pluton is granodioritic to granitic in composition, 60×15 km in dimension and NNW–SSE oriented. Contacts with the granulite basement are variable. To the west (Fig. 4, inset 1), the contacts are progressive: the granitoid is emplaced into the basement as dykes of various thickness and as pegmatitic pods. Most dykes are parallel to the gneissic schistosity. Closer to the main body, boudins of gneiss are incorporated into the granitoids. The passage from the red gneisses to the granitoid is progressive, from gneissic zones with few dykes towards zones where only relics of gneisses inside the granitoids are present. In some places, the granodiorite forms the core of isoclinal folds (Fig. 4, inset 1). In other places, subhorizontal granitoids sills alternate with banded red gneisses. To the east (Fig. 4, inset 2), the contact is sharper. The mineral stretching lineation present in the red gneiss is oblique (45°) to the linear contact. The mafic enclaves into the granitoids are oriented parallel to the contact. Inside the pluton, sinuous bands of foliated facies alternate with non-foliated granitoids. Bands of red gneisses are regularly found in the Ounane structure.

The Ounane pluton main facies is a foliated amphibole granodiorite rarely grading to quartz diorite. K-feldspar is less abundant than plagioclase but forms often large crystals. Microcline is rare. Plagioclase is abundant in the matrix and as large crystals. Biotite is elongated along the foliation. Accessory minerals are rare allanite and oxides. Granites are also present in the Ounane pluton (Abdelhalim, written communication, 1974): (1) a porphyritic syenogranite composed of perthitic microcline, oligoclase, biotite and blue–green hornblende; feldspar mega-crysts (up to 5 cm in length) and Fe–Mg minerals are oriented along the main trend of the massif; (2) a fine-grained biotite–blue–green amphibole-oligoclase–perthitic microcline granite; (3) a fine-grained biotite granite. In these three granitic facies, allanite is abundant and apatite, titanite and zircon are ubiquitous.

The Tisselliline pluton displays an ovoid shape (15×20 km) with the concentric structure of a ring complex (Fig. 4); however the structure of the country-rocks is moulded on it and the Tisselliline concentric structure is folded on its eastern flank (Fig. 4). This feature indicates that granite intrudes into an opening gash in a transpression site. The large-scale fold/gash is thus syn-magmatic and is probably connected with the last, large-scale dextral transpressive displacement along the mega-shear zone just to the east. The present erosion surface is close to the roof of the pluton: a basement slab is a xenolith in the granite. The Tisselliline pluton intruded much higher in the crust than the Ounane pluton, during a brittle movement along the transpressive shear zone.

The main facies is a coarse-grained biotite granite with rare hornblende and with allanite, titanite, magnetite and zircon as common accessory phases. Two other ring complexes have the same mineralogy but medium- or fine-grained (Fig. 4). Two particular facies are present in the Tisselliline pluton: (1) a black granite, with malgachitic (black colour due to minute ferrous hydrates) feldspar, very rich in biotite that forms the second external ring, (2) an orbicular granite present as blobs in the NE part of the pluton. These orbicules form ellipsoids that are more and more elongated eastward towards the shear zone.

3. The Tin Begane garnet-bearing rocks: petrography, *P–T–t* path, age and origin

3.1. Petrography and mineral compositions

The eclogites display symplectitic–kelyphitic textures around garnet (unzoned almandine: alm_{50}, py_{20}, gro_{30}, spe_0). The amphibole (hornblende) is present in several habits: (1) crystallizing within the clinopyroxene–plagioclase (oligoclase An_{12-27}) symplectite in small crystals,

(2) in association with plagioclase (andesine An_{30-36}) around symplectites, (3) elsewhere as larger crystals (<1 mm). The latter are generally oriented along the regional schistosity. The garnet is often large (3–4 mm) and abundant (20%). It shows numerous fractures filled with chlorite, quartz and calcite. The clinopyroxene is a slightly zoned diopside. Jadeite molecule does not attain 5% in the core. The accessory minerals are ilmenite, titanite, rutile and quartz; the secondary minerals are zoisite, calcite and chlorite.

The garnet amphibolites, in addition to amphibole (tschermakite–pargasite) and plagioclase (primary: An_{15}–An_{55}; secondary: An_5–An_{96}) may bear unzoned garnet (alm_{50-65}, py_{7-25}, gro_{13-35}, spe_{0-8}) and/or clinopyroxene (unzoned diopside) as major phases. The schistosity is weak and mainly defined by amphibole, ilmenite and titanite. The other accessory minerals are rutile and magnetite and the secondary minerals are biotite, K-feldspar, calcite and chlorite. The garnet may be fractured in some areas while being intact in others (sample 675). In all areas, veinlets of secondary minerals are rare.

The primary mineral assemblage of the garnet-bearing gneiss is composed of quartz (40–45%), biotite (25–30%), plagioclase (10–15%; oligoclase An_{25-31}), garnet (2–5%; unzoned almandine: alm_{65-69}, py_{19-26}, gro_{4-6}, spe_{3-8}), K-feldspar (<3%), ±sillimanite (0–2%). The accessory minerals are titanite, rutile and tourmaline and the secondary minerals are chlorite (5%) and muscovite (1%).

The metasedimentary rocks are micaschists containing garnet and kyanite with the observed reaction bi + ky ⇒ sill + ms + qtz; quartzites bearing clinopyroxene and amphibole; *marbles* with clinopyroxene, amphibole, forsterite, spinel and biotite.

A complete set of microprobe analyses can be obtained from the authors upon request.

3.2. Paragenetic assemblages and P–T conditions

The eclogite mineral compositions are represented in an Al/(Ca + Na) vs. Ca/(Ca + Na) diagram (Fig. 5). This is not a compatibility diagram and the relationships are not thermodynamically valid. Yet, as all chemical variations occur in the Na–Ca–Al triangle, this diagram helps in understanding the changes in mineralogy that occurred during the PT evolution. The clinopyroxene composition is now diopside, but its occurrence within symplectite together with Na-rich plagioclase suggests that the jadeitic content was much higher at the time of the eclogite facies (with ga + cpx + qtz equilibrium). The primary cpx can be evaluated: the trend of cpx compositions shows that clinopyroxene reacted out with quartz to give plagioclase. On another hand, amphibole crystallizing in the presence of garnet, is likely to have formed from cpx + ga equilibrium. Therefore, the composition of cpx_1 should be close to the intersection between the line joining cpx-II and pl-I and the prolongation of that joining amph-I and ga (Fig. 5), which gives a jadeitic molecule content of 0.3 (0.043 in cpx-II). The different retrogression mineral assemblages can also be displayed in this diagram (Fig. 5)—I: ga–cpx-I–qtz; II: cpx-II–am-I–pl-I–qtz; III: am-II–pl-II–qtz; IV: am-III–zo and not represented in Fig. 5—V: cc–chl–qtz.

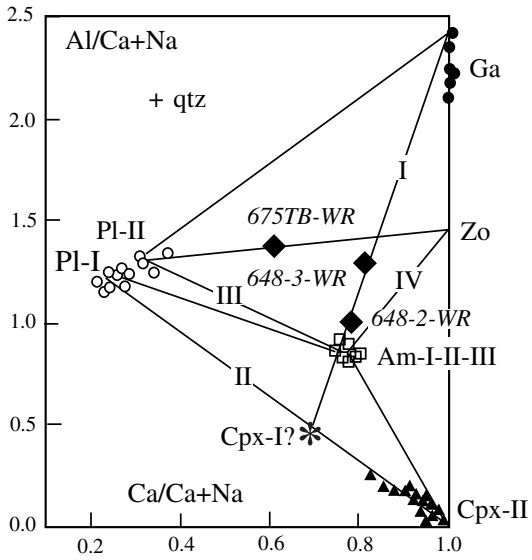

Fig. 5. Al/(Ca + Na) vs. Ca/(Ca + Na) diagram showing the chemical compositions of the mineral phases in the eclogite 680-2b and the different observed mineral assemblages (am = amphibole, cc = calcite, chl = chlorite, cpx = clinopyroxene, ga = garnet, pl = plagioclase, qtz = quartz, zo = zoisite). The whole-rock compositions of studied amphibolites are also located (648-3, 661-1, 675-TB).

The whole-rock compositions of the amphibolites (Table 1) have also been plotted in this diagram. All three compositions belong to the primary ga–cpx-I–pl assemblage but none is within the symplectitic assemblage pl-I–cpx-II–am-I in agreement with garnet in excess. Only the sample 661-1 still bears cpx.

Combining the amphibole–plagioclase thermometer (Holland and Blundy, 1994) with an average calculation using THERMOCALC (Powell and Holland, 1988), the garnet amphibolites give average estimated temperatures of 830 ± 30 °C and pressures of 12 ± 2 kbar while the cpx–garnet amphibolites give 760 ± 30 °C and 11 ± 3 kbar. The eclogite gives a temperature of 790 ± 40 °C (amph-I–cpx-I) using the estimated jadeite content of 0.3, the minimum pressure with the jd–ab–qtz barometer (Holland, 1983) is 15 kbar. THERMOCALC gives average temperature–pressure of 450 ± 25 °C and 4.5 ± 2 kbar for the late retrogression paragenesis cc–chl–am-III–zo–qtz. A summary of the calculated temperatures based on the plagioclase–amphibole pair is plotted in Fig. 6. This figure shows that the differences observed between the calculated temperatures are mostly related

Table 1
Whole-rock geochemistry (major and trace elements) for the Tin Begane rocks, the Ounane and Tisselliline granitoids

Area	Tin Begane				Ounane								Tisselliline				
Type	ga amph		ga–cpx amph	ga-gneiss	granodiorite			granite					granite				
Sample	675	648-3	661-1	648-2	R655	R663	R650	R661	R667	R660	R657	R656	R676	R680	R679	R666	R678
SiO_2	60.47	50.56	49.41	65.80	63.11	63.22	63.37	70.51	72.71	73.10	73.19	73.47	72.93	74.28	74.50	75.99	76.90
TiO_2	0.37	1.42	1.12	0.90	0.70	0.64	0.69	0.45	0.32	0.25	0.21	0.18	0.34	0.26	0.31	0.06	0.13
Al_2O_3	16.64	17.28	15.33	15.64	16.26	15.44	15.48	14.84	13.73	13.62	13.57	13.54	12.47	12.00	12.70	14.06	11.60
Fe_2O_3	3.12	2.01	2.55	1.71													
FeO	4.62	8.34	8.91	4.08													
MnO	0.08	0.12	0.13	0.07	0.08	0.11	0.09	0.03	0.02	0.02	0.03	0.02	0.02	0.02	0.02	0.10	0.01
MgO	3.31	5.07	7.57	2.94	2.49	2.36	2.38	0.78	0.49	0.42	0.33	0.25	0.30	0.23	0.25	0.03	0.05
CaO	8.03	11.60	12.03	2.67	4.76	4.17	4.49	1.80	1.34	1.26	1.15	1.07	0.47	0.53	0.87	0.44	0.38
Na_2O	2.75	1.48	1.94	3.20	2.81	5.01	3.08	3.24	3.40	3.13	3.06	3.37	2.90	3.21	2.90	3.26	3.26
K_2O	0.24	0.38	0.13	2.07	3.05	2.71	2.72	4.90	5.18	5.74	5.63	5.42	5.84	6.05	5.72	4.01	6.35
P_2O_5	0.05	0.12	0.08	0.14	0.20	0.18	0.21	0.12	0.06	0.04	0.02	0.01	0.06	0.01	0.01	0.01	0.01
P.F.	1.00	1.84	1.40	1.50	0.64	0.89	1.01	0.54	0.51	0.49	0.70	0.52	0.86	1.00	0.71	0.41	1.00
Total	100.68	100.22	100.60	100.72	99.89	100.48	99.05	100.26	100.02	100.13	99.78	99.58	99.01	99.57	99.94	98.97	100.11
Fe_2O_{3t}	8.25	11.26	12.45	6.24	5.79	5.75	5.53	3.05	2.26	2.06	1.89	1.73	2.82	1.98	1.95	0.60	0.42
V	187	267	265	123	84	74	78	24	15.6	11.4	13.3	8.6	9.20	2.51	5.02	1.15	2.28
Rb	7.24	20.6	1.30	68	81	143	109	158	176	140	177	244	136	187	167	452	180
Sr	184	69		184	617	419	487	238	172	209	162	126	173	76	98	11.3	46
Y	17.4	32.4	19.7	31.8	26.3	28.7	25.8	12.9	17.7	8.9	16.8	27.3	27.4	4.8	25.8	52.9	18.4
Zr	17	68	48	170	176	153	135	259	180	174	148	141	321	58	212	41	219
Nb	2.3	6.3	3.0	11	17.0	15.5	13.1	11.2	12.4	7.1	14.1	20.02	9.9	6.2	16.6	52.1	10.3
Ba	253	225	6	420	2124	1243	1365	1416	977	1378	809	656	942	337	624	84	181
La	2.03	3.32	3.58	24.3	68	44	40	104	93	83	77	69	178	9.1	181	14.4	146
Ce	4.59	9.05	8.78	54.0	135	89.8	76.8	209	191	166	151	141	347	15.8	305	38.0	289
Pr	0.67	1.48	1.21	5.96	14.0	9.45	8.36	21.5	19.8	15.9	14.7	13.7	34.8	1.59	33.7	4.78	30.0
Nd	3.46	8.02	6.07	23.2	45.8	31.6	28.5	66.9	62.5	47.4	44.7	43.1	107	4.93	102	20.5	89.8
Sm	0.96	2.66	1.82	4.57	6.76	5.45	4.73	8.15	9.27	6.27	6.37	6.96	14.9	0.90	14.4	6.06	13.0
Eu	0.35	1.17	0.86	1.19	1.63	1.09	1.20	1.09	0.93	0.65	0.74	0.54	1.13	0.68	0.96	0.04	0.41
Gd	1.54	3.60	2.22	4.2	5.83	5.05	3.92	4.58	5.78	4.28	4.73	5.69	10.78	0.75	9.84	5.72	8.12
Dy	2.10	4.23	2.64	4.18	4.11	4.51	3.57	2.36	3.53	1.82	2.92	4.35	5.78	0.92	5.23	7.70	4.17
Ho	0.48	0.96	0.59	0.9	0.77	0.91	0.70	0.34	0.55	0.20	0.47	0.75	0.95	0.20	0.86	1.53	0.62
Er	1.49	2.65	1.58	2.43	2.27	2.42	2.04	0.71	1.14	0.46	1.28	2.17	2.10	0.49	1.90	4.78	1.20
Yb	1.48	2.46	1.39	2.26	1.79	2.08	1.78	0.50	0.82	0.31	1.03	1.69	1.25	0.68	1.20	4.76	0.69
Lu	0.22	0.37	0.21	0.35	0.24	0.28	0.26	0.05	0.11	0.04	0.13	0.22	0.17	0.10	0.15	0.78	0.06
Hf	0.83	2.15	1.50	4.12	5.11	4.61	3.70	7.79	5.70	5.80	5.10	4.98	9.44	3.24	6.79	3.54	7.32
Ta	0.24	0.49	0.31	0.91	0.93	1.03	1.06	0.98	1.23	0.51	1.15	2.45	0.23	0.30	0.58	4.90	0.28
W	0.12	1.13	0.35	0.47	0.28	0.12	0.36	0.10	0.32	0.11	0.10	0.10	0.42	0.05	0.12	0.68	0.10
Pb	7.8	11.7	8.8	16.0	20.8	19.2	21.1	30.3	35.2	29.5	36.6	39.7	25.2	30.9	27.8	42.1	24.5
Th	0.34	1.18	0.34	5.73	12.1	14.7	7.79	17.5	26.3	24.9	32.1	29.6	23.6	7.87	30.1	15.5	32.6
U	0.25	0.53	0.15	2.51	1.66	2.01	2.58	0.98	1.82	2.11	3.55	3.99	1.88	1.57	1.65	5.75	1.43

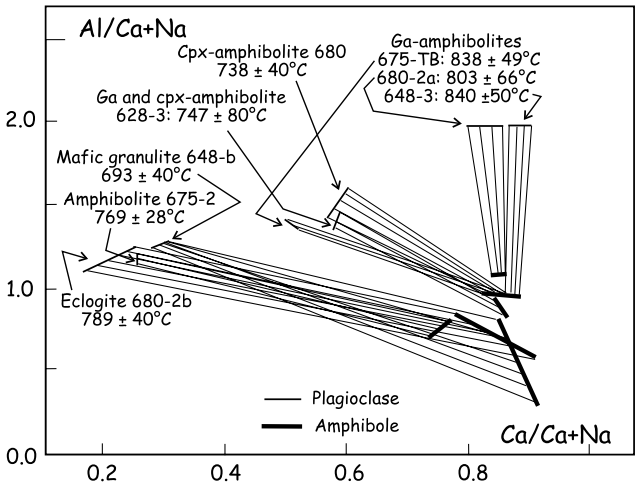

Fig. 6. Al/(Ca + Na) vs. Ca/(Ca + Na) diagram showing the different amphibole–plagioclase couples from the amphibolites and the eclogite and the obtained temperatures.

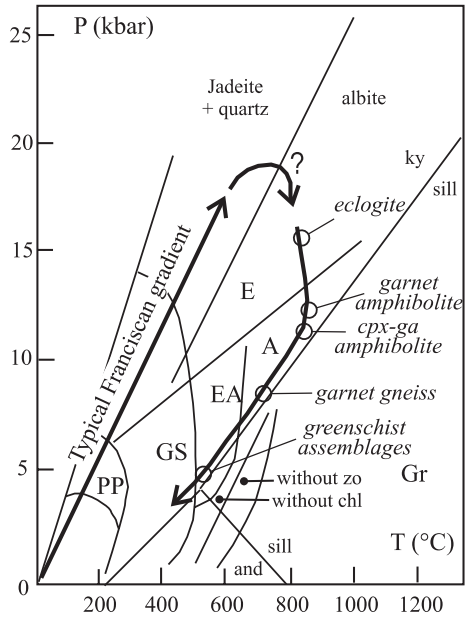

Fig. 7. *P–T–t* path obtained from the different sample studied (eclogite, garnet amphibolite, cpx–garnet amphibolite, gneiss). Ky = kyanite; sill = sillimanite; and = andalusite; zo = zoisite; chl = chlorite. Different metamorphic facies from Spear (1993): Z = zeolite; PP = prehnite–pumpellyite; GS = greenschist; EA = epidote amphibolite; A = amphibolite; E = eclogite; Gr = granulite.

to the different plagioclase compositions in rocks of different bulk compositions.

The gneiss 648-2 gives a temperature of 695 ± 54 °C (ga–bi pair; Williams and Grambling, 1991). THERMOCALC assigns 8 ± 3 kbar and 700 ± 50 °C to the ga–bi–pl–Kf assemblage. The micaschists give temperatures between 577 ± 30 and 593 ± 50 °C (ga–bi couple; Williams and Grambling, 1991). Thermocalc gives a temperature of 575 ± 30 °C and a pressure of 4 ± 2 kbar with the ga–bi–ky–pl–Kf–qtz assemblage.

All the studied rocks belong to a same *P–T–t* path (Fig. 7): the various compositions retain different *P–T* conditions or the exhumation process has stripped samples from different depths. It is worth noting that this retrogression path (1) is bracketed by the primary and the latest paragenesis found in the eclogite, (2) lies always within the kyanite field. This path is consistent with the retrogression part of a loop whose prograde path corresponds to a typical subduction (Franciscan) gradient (Fig. 7).

3.3. Sm–Nd geochronology and garnet trace element composition

Five samples, studied in detail for the mineralogy and for metamorphic parageneses, have been selected for Sm–Nd dating (Table 2): one eclogite (680-2b), three garnet amphibolites (675TB, 661-1 and 648-3) and one garnet-bearing gneiss (648-2). Mineral separates (>99% purity) have been obtained after crushing, magnetic separation and final grain-by-grain manual separation under the binocular. Altered or ambiguous grains have been systematically discarded. It was not possible to separate some phases such as the clinopyroxene from the symplectites. Between 50 and 150 mg of minerals were used for isotopic measurements (see analytical techniques in Appendix A). The age calculations (isochrons and weighted means) follow Ludwig (1999), when MSWD > 1.2, errors on the age are multiplied by $\sqrt{\text{MSWD}}$.

Even if very pure, the garnet concentrates gave low Sm/Nd in some samples, sometimes lower than the whole rock. The garnet was then analyzed by laser ablation coupled to an ICP-MS (Table 4; see analytical techniques in Appendix A) for trace elements in order to determine the elements linked to the variation of the Sm/Nd ratios and to precise the process at the origin of this geochemical modification. Systematic sections across garnet grains were performed. Means of similar patterns are provided in figures for clarity (number of spots used for each mean is given in Fig. 8 and Table 4). Variations observed in the garnet spots do not seem to be due to inclusions, not seen under the microscope but also not measured: garnets with peculiar REE patterns have similar concentrations in most of the other trace elements (Table 4), only U and Th seem to follow the REE behaviour.

The garnet amphibolite 675-TB has homogeneous and typical REE in garnet (Fig. 8A) with a strong depletion in light REE (LREE) and enrichment in heavy REE (HREE). Yb_N/Ce_N varies from 240 to 1500. The 50 patterns measured could be reduced to one pattern without detriment, close to the isotope dilution (ID) Sm and Nd values, representing the mean concentrations of ≈50–100 mg garnet. The slightly higher ID values are

Table 2
Sm–Nd isotopes on whole rock and minerals and Rb–Sr isotopes on whole rock for the Tin Begane rocks

Sample	Sm	Nd	$^{147}Sm/^{144}Nd$	$^{143}Nd/^{144}Nd$	2σ	ε_{Nd}			T_{DM}	$^{87}Rb/^{86}Sr$	$^{87}Sr/^{86}Sr$	2σ	Sr_i	
						0 Ma	515 Ma	685 Ma					515	685
680-2b WR	5.422	19.40	0.1691	0.512419	0.000010	−4.27	−2.46	−1.85	–	0.1985	0.717954	0.000025	0.716497	0.716014
680-2b ga	3.574	14.15	0.1528	0.512355	0.000014	−5.52	−2.63	−1.67						
680-2b am	10.79	34.46	0.1893	0.512515	0.000005	−2.40	−1.92	−1.76						
680-2b pl	2.309	9.518	0.1467	0.512219	0.000012	−8.17	−4.89	−3.80						
675-TB WR	1.284	3.715	0.2091	0.512925	0.000017	5.60	4.79	4.52	–	0.1396	0.705118	0.000011	0.704093	0.703753
675-TB am	3.413	9.034	0.2285	0.513006	0.000009	7.18	5.09	4.40						
675-TB ga	0.419	0.402	0.6307	0.514820	0.000030	42.6	14.0	4.56						
675-TB pl	0.054	0.336	0.0972	0.512453	0.000048	−3.61	2.94	5.11						
661-1 WR	1.82	6.07	0.1814	0.512683	0.000010	0.88	1.89	2.23	–					
661-1 ga	1.352	2.662	0.3072	0.513121	0.000019	9.42	2.15	−0.26						
661-1 pl	0.24	1.614	0.0899	0.512401	0.000017	−4.62	2.41	4.74						
661-1 am	1.741	5.213	0.2020	0.512763	0.000013	2.44	2.09	1.98						
661-1 cpx	0.308	1.038	0.1795	0.512672	0.000008	0.66	1.80	2.18						
648-3 WR	2.231	9.878	0.1366	0.512399	0.000013	−4.66	−0.71	0.60	1270	1.564	0.743613	0.000011	0.732132	0.728324
648-3 ga	2.704	9.044	0.1808	0.512552	0.000014	−1.68	−0.63	−0.29						
648-3 am	11.93	51.11	0.1411	0.512475	0.000006	−3.18	0.48	1.69						
648-3 chl	3.303	14.50	0.1378	0.512670	0.000008	0.62	4.51	5.79						
648-2 WR	5.584	26.07	0.1296	0.512351	0.000014	−5.60	−1.18	0.28	1252	1.036	0.717351	0.000009	0.709745	0.707222
648-2 bi	3.962	19.38	0.1237	0.512325	0.000013	−6.11	−1.30	0.29						
648-2 ga	3.284	10.43	0.1905	0.512554	0.000011	−1.64	−1.23	−1.10						
648-2 pl	0.059	0.696	0.0513	0.512313	0.000014	−6.34	3.24	6.41						

T_{DM} are given for whole rocks having $^{147}Sm/^{144}Nd < 0.15$.

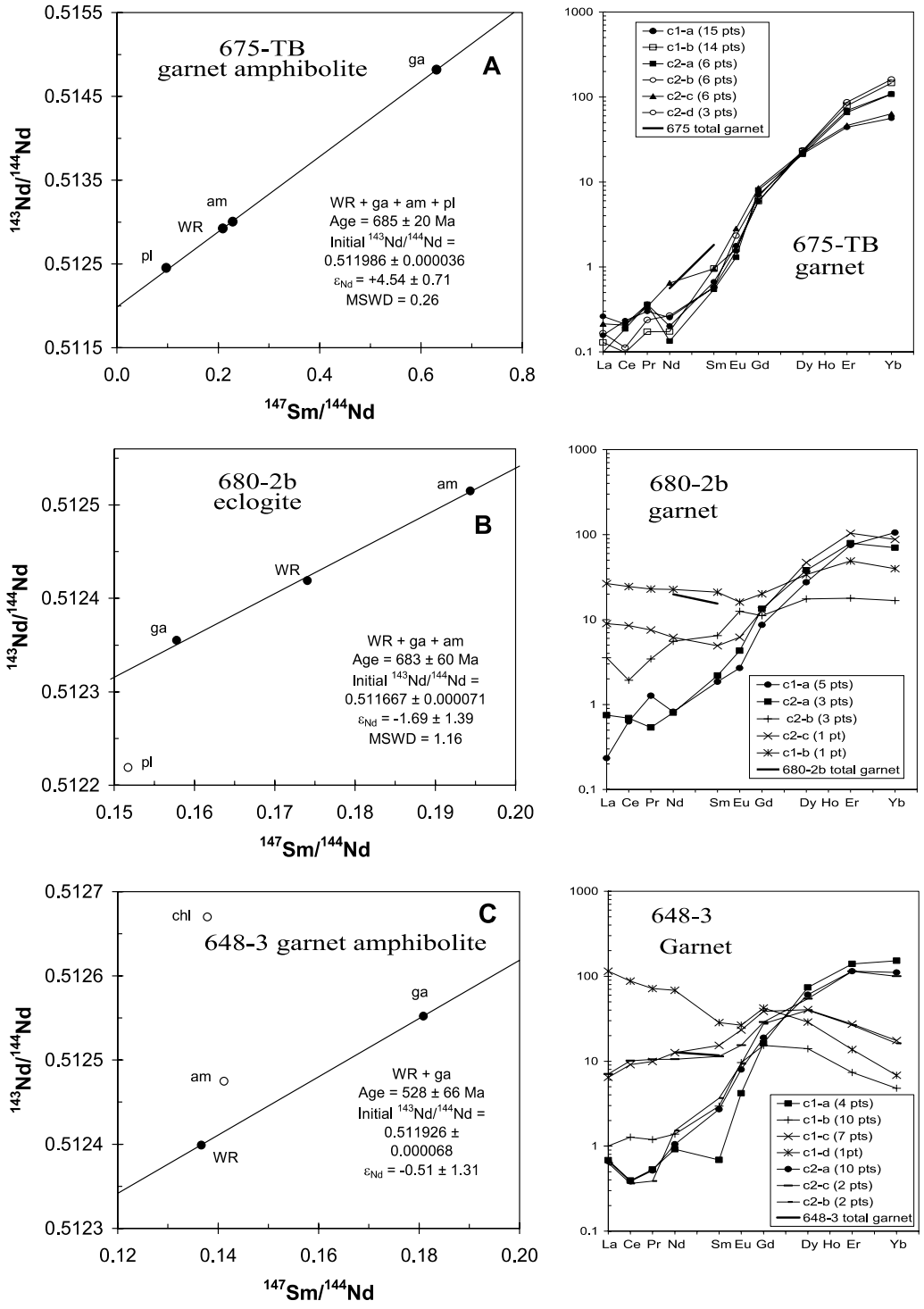

Fig. 8. Sm–Nd isochrons on minerals and REE on garnet from the Tin Begane area: (A) 675-TB garnet amphibolite; (B) 680-2B eclogite; (C) 648-3 garnet amphibolite; (D) 661-1 garnet amphibolite; (E) 648-2 garnet gneiss.

probably due to a slight underevaluation of LA-ICP-MS of Sm and Nd, a little low when compared to adjacent rare earths. These patterns are representative of the amphibolite-facies metamorphism with no retrogression effects. All the analysed minerals and the whole rock from the 675-TB garnet amphibolite determine an isochron: 685 ± 20 Ma, $\varepsilon_{Nd} = +4.54 \pm 0.71$, MSWD $= 0.26$ (Fig. 8A). The minerals from this sample are crack-free and very poor in secondary minerals. This age of 685 ± 20 Ma can only correspond to the amphibolite-facies metamorphism which produced the analyzed minerals.

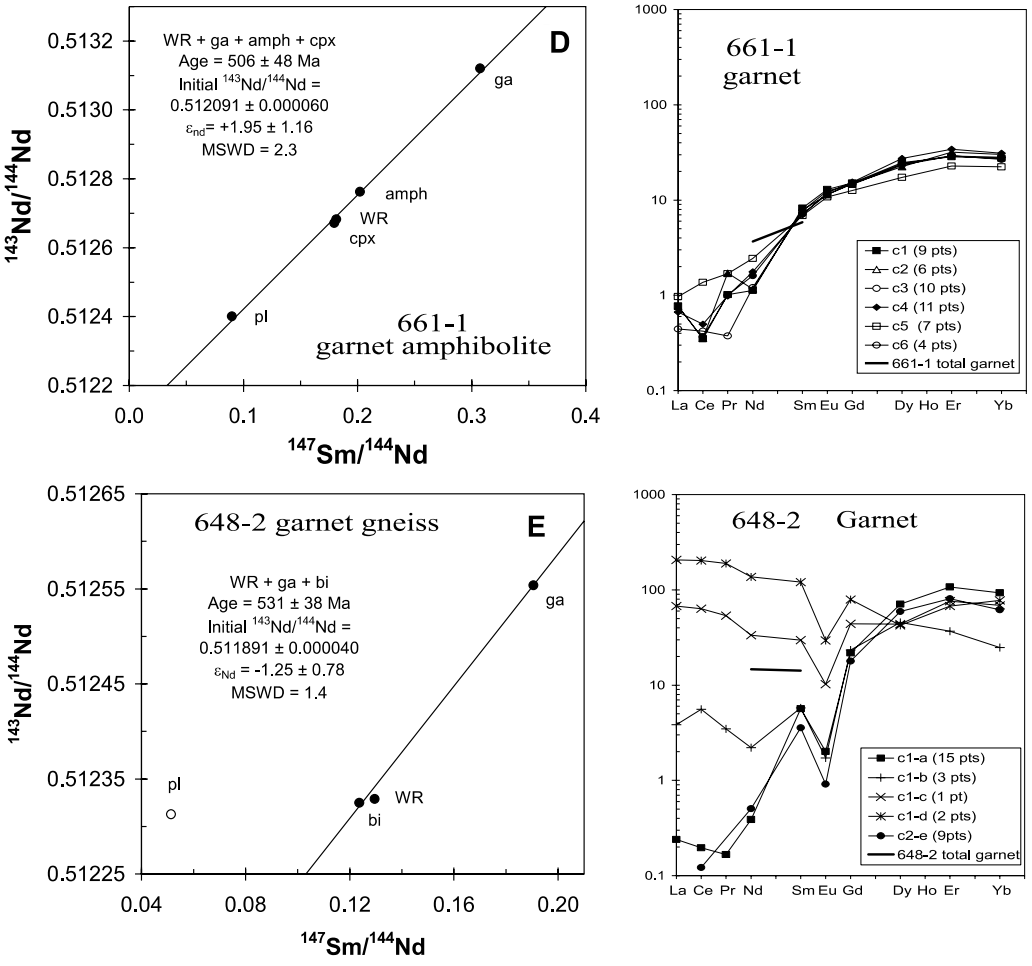

Fig. 8 (*continued*)

The eclogite 680-2b displays several kinds of REE patterns in its garnets, found in all analyzed crystals (Fig. 8B): each of them possess different zones that are more or less primitive. Some parts (c1a and c2b) have REE patterns similar to that of 675-TB ($Yb_N/Ce_N = 101–168$) but also patterns showing enrichment in LREE and depletion in HREE ($Yb_N/Ce_N = 1.6–10$). Let us note that these two phenomena are not correlated: c2-c is more than 10 times enriched in LREE but it has still high HREE ($Ce_N = 8.5$; $Yb_N = 87.5$) while c2-b shows both phenomena ($Ce_N = 1.9$; $Yb_N = 16.7$). LREE enrichment is more important than HREE depletion. The enriched zones impose their signature to the global garnet population as shown by the isotope dilution bulk values (Fig. 8B). The whole rock (WR), garnet and amphibole from the eclogite 680-2B determine an isochron: 683 ± 60 Ma, $\varepsilon_{Nd} = -1.69 \pm 1.39$, MSWD = 1.16 (Fig. 8B). The low $^{147}Sm/^{144}Nd$ of the garnet (0.15, lower than the whole rock, generating the low precision of the isochron) suggests a REE readjustment in agreement with the presence of the amphibole on the same isochron. This indicates that the age obtained corresponds to that of the amphibolite facies acquired during the early thrusting. The plagioclase from the symplectite, then a secondary phase, lies well below the isochron (2ε) and this has no clear explanation.

The garnet amphibolite 648-3 shows primary and re-equilibrated REE patterns in its garnets (Fig. 8D). C1-a and C2-a have primitive characteristics ($Yb_N/Ce_N = 280–290$). In this rock also, the LREE enrichment is not correlated to the HREE depletion: c1-b and c2-b have low REE and low HREE ($Ce_N = 0.36–1.28$; $Yb_N = 4.8–16$), c2-c has high LREE and high HREE ($Ce_N = 10$; $Yb_N = 100$), c1-c and c1-d have high LREE and low HREE ($Ce_N = 9$ and 87; $Yb_N = 7$ and 17). The isotope dilution on the bulk garnet is within the range given by the LA-ICP-MS but is largely influenced by the enriched zones. The 648-3 garnet amphibolite, relatively rich in

chlorite, does not give aligned minerals (Fig. 8D). Only a WR-garnet age can be calculated at 528 ± 66 Ma with $\varepsilon_{Nd} = -0.51 \pm 1.31$. The chlorite and the amphibole lie well above the WR-ga line. The low $^{147}Sm/^{144}Nd$ of the garnet indicates that this mineral has been reset at ≈530 Ma. This means that it has lost a large part of the radiogenic Nd produced before the lowering of its Sm/Nd. The high position of the chlorite above the isochron suggests that it could have acted as a pump for moving radiogenic Nd, as K-feldspar acts for radiogenic Pb. Let us note that this chlorite has an $\varepsilon_{Nd} = +4.6$ at 530 Ma, a value similar to that of the 675-TB amphibolite at the same age ($\varepsilon_{Nd} = +4.8$; Table 2). The amphibole, also a hydrated mineral, could have acted in the same way but its higher Nd concentration (51 ppm Nd) would have diluted the effect. This suggests a clearly positive ε_{Nd} for rock 648-3 at ≈685 Ma.

The garnet-clinopyroxene amphibolite 661-1 (Fig. 8C) has homogeneous and quite typical REE patterns in garnet although less fractionated (Yb_N/Ce_N from 16 to 85) than the sample 675TB due to both higher LREE ($Ce_N = 0.35$–1.37 vs. 0.10–0.26 for 675-TB) and lower LREE ($Yb_N = 22$–30 vs. 50–160 for 675-TB). LREE show disturbances. This can be probably ascribed partly but not entirely to the bigger analytical errors at these lower concentrations. All the analysed minerals (ga, pl, cpx, amph) and the whole rock from 661-1 ga and cpx amphibolite nearly determine an isochron: 506 ± 48 Ma, $\varepsilon_{Nd} = +1.95 \pm 1.16$, MSWD = 2.3 (Fig. 8C). Although the minerals from this sample are relatively poor in secondary phases, the age obtained is much younger than the two former ones and can only be ascribed to a regression event. The bulk isotope dilution concentrations are higher than those measured by laser ablation. This suggests the existence within the 50 mg of garnet analyzed for Sm–Nd dating of parts of grains having enriched REE spectra as in sample 648-3, which have a major influence on the bulk concentrations. This could explain the young age observed.

The gneiss 648-2 displays also variations in its garnets (Fig. 8E) from primitive to redistributed REE patterns ($Yb_N/Ce_N = 0.4$–500) but affecting mainly the LREE (Ce_N varies from 0.12 to 63 and Yb_N from 25 to 93). The garnet in this rock shows a pronounced negative Eu anomaly. The global concentration given by isotope dilution on bulk garnet is largely influenced by the redistributed garnet enriched parts. The Sm–Nd age has then to be ascribed to the greenschist facies. The gneiss 648-2 defines an isochron with the WR, biotite and garnet: 531 ± 38 Ma, $\varepsilon_{Nd} = -1.25 \pm 0.78$, MSWD = 1.4 (Fig. 8E). The plagioclase lies well above this isochron with an $\varepsilon_{Nd} = +3.52$ at 530 Ma (Table 2), in the same range as 675 TB and 648-3 chlorite at the same age. This suggests that, in contrast to garnet, plagioclase retained the ε_{Nd} of the amphibolite facies. As for sample 648-3, this would suggest a positive ε_{Nd} for this gneiss at ≈685 Ma.

Two sets of ages have been determined in the Tin Begane area that can be reduced to two weighted means (following Ludwig, 1999): 685 ± 19 Ma (MSWD = 0.01) and 522 ± 27 Ma (MSWD = 0.41). The first age corresponds to the amphibolite facies (retrogressed conditions for the eclogite) and the second one to the end of the Laouni greenschist facies metamorphic conditions. This event is also marked by the intrusion of high-level granitic and leucogranitic plutons (535–525 Ma; Cheilletz et al., 1992; Azzouni-Sekkal et al., 2003, this issue). Wet metamorphic retrogression is then a major cause of REE mobility in garnet.

3.4. The origin of the Tin Begane thrust sheets

All the studied rocks belong to the same *P–T–t* path, consistent with the retrogression part of a loop whose prograde path would correspond to a typical Franciscan gradient (Fig. 7). Such a gradient indicates a subduction environment (e.g. Peacock, 1993 and references therein). This is compatible with the whole-rock chemistry of the studied samples (Table 1; Fig. 9): they show enrichment in K, Rb, Ba and depletion in HFS elements (Fig. 9A) suggesting an island arc environment for the amphibolite protoliths and a more mature active margin for the protolith of the gneiss 648-2. The sample 661 has a composition closer to MORB, although slightly depleted in HFSE. The rare earth elements (Fig. 9B) are variable from nearly flat (648-3) with positive Eu anomaly (661-1) to enriched in LREE (paragneiss 648-2). Combined convex upward spectra, positive Eu anomaly and low REE abundance indicate that the REE budget is mainly controlled by cpx and plagioclase as shown by the laser spots (Fig. 9C; laser ablation coupled to an ICP-MS; Table 4). The sample 675TB spectrum shows in addition the influence of garnet (HREE enrichment). The available whole-rock geochemical analyses are too few to constrain the palaeoenvironment of the Tin Begane amphibolites and associated rocks, but a former subduction zone is likely.

The rare earth elements have been redistributed during the different metamorphic phases that have affected variably the studied rocks. Calculated ε_{Nd} relate to the metamorphic phase dated. The estimate of the ε_{Nd} of the protolith is then model-dependent and has to be coupled to the depleted model age (T_{DM}) information.

The garnet amphibolite 675-TB whole rock has a $^{147}Sm/^{144}Nd$ (0.209) close to that of the depleted mantle (0.214–0.230). This gives subparallel evolution with time of the $^{143}Nd/^{144}Nd$ of the rock and the depleted mantle, giving a meaningless T_{DM} value but also a fairly constant ε_{Nd} whatever the age considered (+5.6 now, +4.5 at 685 Ma). This value indicates no or slight participation of a pre-Neoproterozoic crust in this rock although it contains 60% SiO_2 (tonalite in the Q'-Anor diagram of Streckeisen and Le Maitre, 1979). Coupled with the

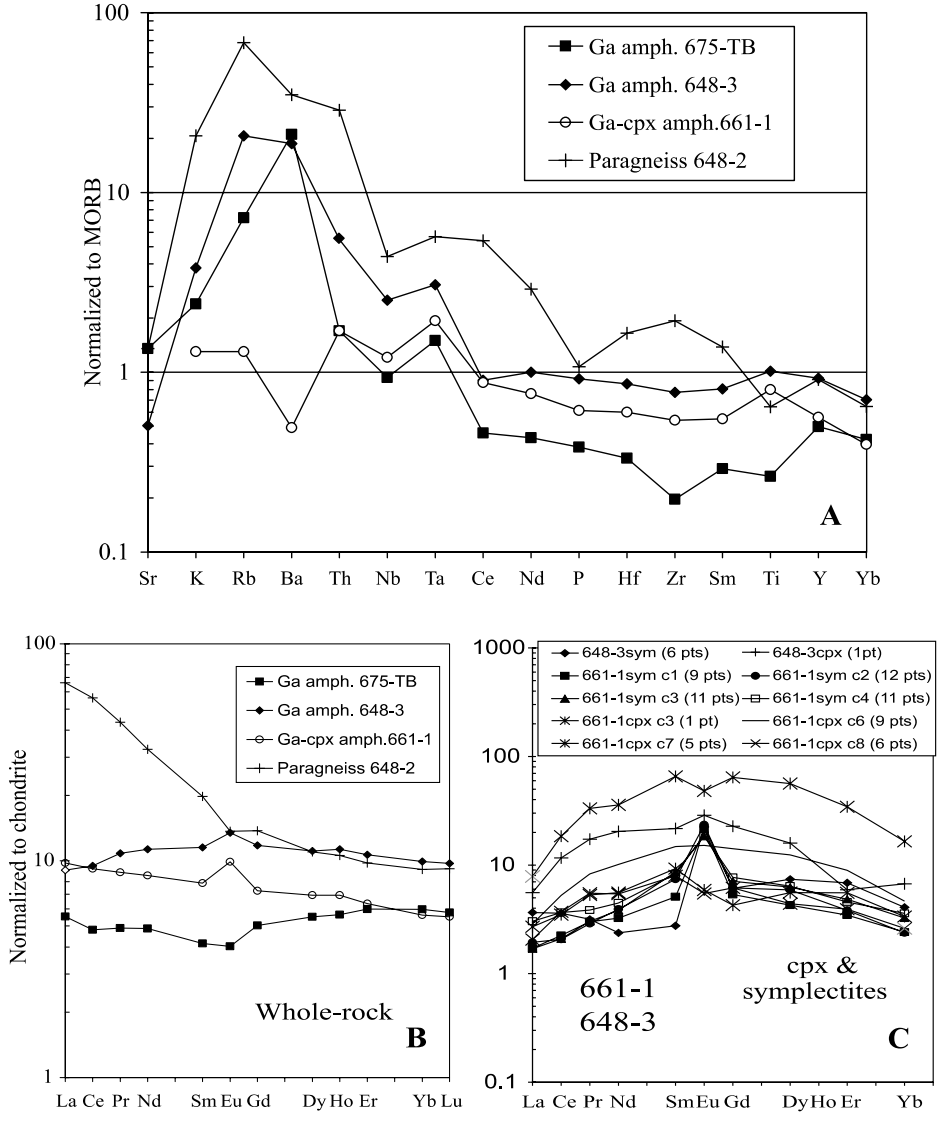

Fig. 9. Chemistry of studied Tin Begane rocks and minerals: (A) spidergram normalized to MORB (Pearce, 1982) on whole-rock; (B) REE on whole-rock normalized to chondrite (Taylor and Mc Lennan, 1985); (C) REE on cpx and cpx–plag symplectite.

geochemical data, this suggests that it belongs to an island arc TTG series. The eclogite 680-2b provides a WR $\varepsilon_{Nd} = -1.8$ at 685 Ma; $^{147}Sm/^{144}Nd$ (0.17) is too high to give a useful T_{DM}. The garnet amphibolite 661-1 has a WR ε_{Nd} of +1.92 (isochron: +1.97) at 502 Ma and +2.23 at 685 Ma. $^{147}Sm/^{144}Nd$ (0.18) is also too high to give a meaningful T_{DM} value. The garnet amphibolite 648-3 (metadiorite) and the garnet gneiss 648-2 (metagranodiorite or metagreywacke) bring similar constraints: they have for whole rock at 530 Ma $\varepsilon_{Nd} = -0.6$ and -1.5 and $T_{DM} = 1270 \pm 38$ Ma and 1291 ± 63 Ma, respectively. ε_{Nd} calculated back to 685 Ma are +0.6 for 648-3 and −0.1 for 648-2 (Table 2). Considering chlorite ε_{Nd} for the sample 648-3 (+4.6 at 530 Ma) and plagioclase ε_{Nd} from sample the 648-2 (+3.5 at 530 Ma), and taking the WR Sm/Nd, ε_{Nd} would have been +5.8 and +5.1 at 685 Ma, for samples 648-3 and 648-2, respectively. This is close to the $\varepsilon_{Nd} = +4.5$ of sample 675TB. Mean ε_{Nd} for the Tin Begane thrust sheets can then be evaluated at +5 at 685 Ma. This indicates a major juvenile component within all the rock studied. Coupled with their geochemistry, this favours an island arc origin in an oceanic setting.

This subduction-related geodynamic environment can be related to that of the nearby Mount Tessalit ophiolites (Fig. 2).

4. The Ounane and Tisselliline granitoids from the Gour Oumelalen area: age and origin

The whole-rock geochemical analyses are listed in Table 1 and the Sr–Nd isotopic results in Table 3. Analytical techniques are given in Appendix A.

Table 3
Sm–Nd and Rb–Sr isotopes on whole rock for the Ounane and Tisselliline granitoids

Sample	Sm	Nd	$^{147}Sm/^{144}Nd$	$^{143}Nd/^{144}Nd$	2σ	ε_{Nd}		T_{DM}	Rb	Sr	$^{87}Rb/^{86}Sr$	$^{87}Sr/^{86}Sr$	2σ	Sr_i	
						0 Ma	555 Ma	624 Ma						555 Ma	624 Ma
Ounane															
R656	6.96	43.05	0.0978	0.511369	0.000008	−24.75	−17.76	−16.89	1949	244	126	5.65	0.75739	0.000008	0.712673	0.707089
R655	6.76	45.82	0.0892	0.511475	0.000008	−22.69	−15.09	−14.14	1646	81	617	0.38	0.711711	0.000009	0.708716	0.708342
R650	4.73	28.47	0.1004	0.511164	0.000009	−28.75	−21.95	−21.10	2322	109	487	0.65	0.714263	0.000007	0.709135	0.708494
R660	6.27	47.38	0.0800	0.511165	0.000008	−28.73	−20.49	−19.46	1919	140	209	1.94	0.725869	0.000007	0.710534	0.708619
R661	8.15	66.92	0.0737	0.511232	0.000008	−27.43	−18.73	−17.64	1737	158	238	1.93	0.725630	0.000007	0.710371	0.708466
R667	9.27	62.45	0.0898	0.511228	0.000008	−27.5	−19.9	−19.01	2003	176	172	2.96	0.734746	0.000007	0.711296	0.708367
R657	6.37	44.74	0.0860	0.511361	0.000010	−24.91	−17.09	−16.11	1755	177	162	3.18	0.738354	0.000007	0.713200	0.710059
R663	5.45	31.56	0.1043	0.511532	0.000008	−21.57	−15.04	−14.23	1820	143	419	0.99	0.715347	0.000008	0.707523	0.706546
Tisselliline																
R666	6.06	20.49	0.1789	0.511882	0.000012	−14.75	−13.50	−13.35	–	452	11	127.2	1.700553	0.000013	0.694140	0.568463
R676	14.93	106.5	0.0848	0.511451	0.000013	−23.15	−15.24	−14.25	1613	136.1	172.6	2.29	0.72513	0.000007	0.707045	0.704786
R678	12.96	89.81	0.0873	0.511504	0.000005	−22.12	−14.38	−13.41	1576	180.4	45.9	11.47	0.796441	0.000011	0.705665	0.694329
R679	14.44	101.9	0.0857	0.511511	0.000008	−21.98	−14.13	−13.15	1545	167	98	4.92	0.746994	0.000007	0.708062	0.703201
R680	0.8971	4.9292	0.1100	0.511653	0.000013	−19.21	−13.09	−12.32	1728	186.5	76.3	7.11	0.764584	0.000008	0.708305	0.701277

T_{DM} are given for whole rocks having $^{147}Sm/^{144}Nd < 0.15$.

4.1. Rb–Sr geochronology

Eight samples from the Ounane pluton have been analyzed for the Rb–Sr geochronology. The isochron obtained has a high MSWD of 19 giving an age of 628 ± 47 Ma (initial $^{87}Sr/^{86}Sr$ or $Sr_i = 0.7081 \pm 0.0016$; Fig. 10A). This high MSWD is due to two samples (R657 and R663). Based on the other six samples, the age obtained is: 624 ± 15 Ma ($Sr_i = 0.70839 \pm 0.00016$; MSWD = 0.87; 6WR/8; Fig. 10A). These two ages and Sr_i are very similar, suggesting slight variation of initial ratio in the two outliers, which suggests that the second more precise age is meaningful.

The five samples from Tisselliline pluton are well aligned, determining an isochron: 555 ± 15 Ma, $Sr_i = 0.70728 \pm 0.00095$, MSWD = 1.16 (Fig. 10B). The sample R666 possesses a much higher Rb/Sr than the other samples. However, the four other samples determine similar parameters, although less precise: 560 ± 21 Ma ($Sr_i = 0.7070 \pm 0.0012$; MSWD = 1.4).

The age of the Ounane pluton is in the range known for batholiths in the Laouni terrane (600–610 Ma; Bertrand et al., 1986) and in other parts of the shield (620–580 Ma; Boullier, 1991 and references therein). This age corresponds to the beginning of movements along shear zones following collision with the West African craton (Liégeois et al., 1998) that occurred at ≈620 Ma (Jahn et al., 2001). To the east, in the Assodé-Issalane terrane, high-K calc-alkaline batholiths have been dated within the 645–580 Ma age range (Liégeois et al., 1994).

The age of the Tisselliline pluton is younger than the recorded ages of the high-K calc-alkaline batholiths (625–580 Ma) and older than the Taourirt high-level plutons located on the western age of LATEA (530–520 Ma). The Taourirt plutons intruded at the end of the transtensive deformation along the 4°50′ shear zone (Djouadi et al., 1997; Paquette et al., 1998; Azzouni-Sekkal et al., 2003, this issue). Structural observations indicate that the Tisselliline pluton intruded high in the crust but under a transpressional regime (Latouche, 1975) and has not been included in the Taourirt family by Boissonnas (1974). This intermediate age appears in agreement with these data. On the other hand, it is contemporaneous to the alkaline–peralkaline subvolcanic province in the Adrar des Iforas (Kidal terrane; Liégeois et al., 1987), in particular the Tessalit ring complex (553 ± 8 Ma; Liégeois et al., 1996). This indicates that during the period from 560–520 Ma, characterized by high-level intrusions, the Tuareg shield was already largely eroded.

4.2. Major and trace element geochemistry

The Ounane and Tisselliline plutons are enriched in K_2O (Fig. 11A). The Ounane defines a high-K calc-alkaline trend, incomplete due to the number of samples

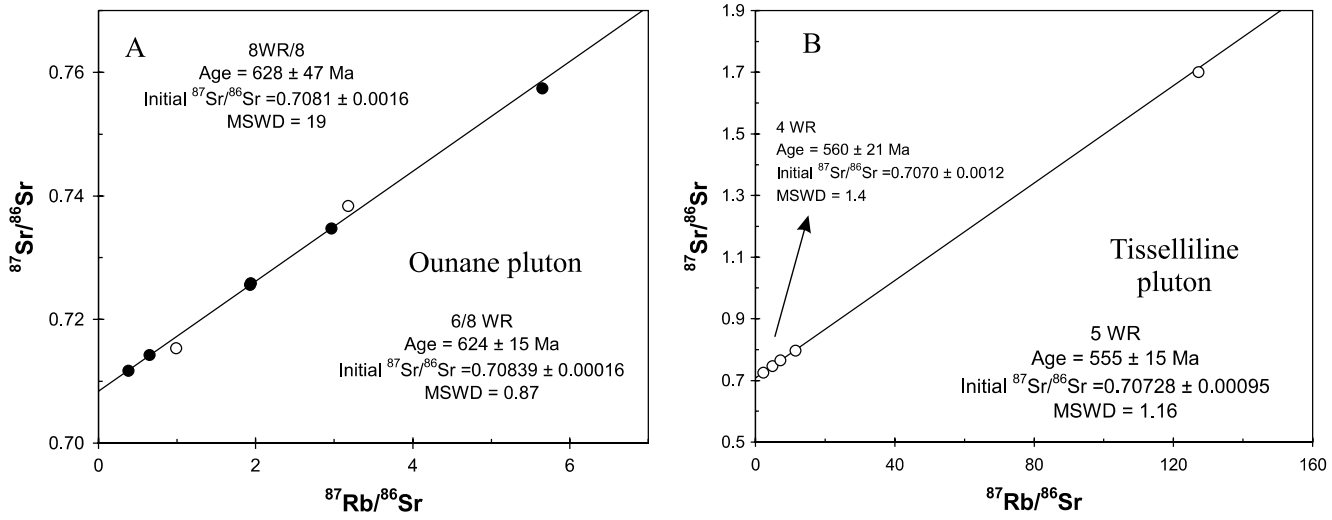

Fig. 10. Rb–Sr isochrons for the Ounane pluton (A) and the Tisselliline pluton (B).

but within the Kidal-Assodé HKCA syn-shear group (640–580 Ma; Liégeois et al., 1998). The Tisselliline is composed only of granites and for such differentiated rocks, the geochemistry of HKCA and alkaline series share several characteristics, including K_2O content (Liégeois et al., 1998). Indeed, the Tisselliline granitoids are located at the intersection of the potassic and alkaline trends (Fig. 11A). The sample R666 is particularly low in K_2O. The agpaitic index (molar $[Na_2O + K_2O]/Al_2O_3$) better discriminates HKCA series from alkaline–peralkaline series (Fig. 11B): above 1, the rock is peralkaline while metaluminous alkaline granitoids have generally an agpaitic index AI > 0.87, in contrast to the HKCA granitoids (Liégeois and Black, 1987). In that diagram, the Ounane granitoids are always <0.87, in agreement with their HKCA character; with the exception again of R666, the Tisselliline granitoids have AI > 0.87 with the sample R678 being peralkaline (AI = 1.05) suggesting they belong to an alkaline–peralkaline series. This is confirmed by the use of the sliding normalization to the reference alkali-calcic Yenchichi–Telabit series: each studied sample is normalized to an interpolated rock of the reference series having the same SiO_2 content, to minimize the differentiation effect (Liégeois et al., 1998). In the synthesis diagram grouping some LILE (+Ta) on the *Y*-axis and some HFSE on the *X*-axis (Fig. 11C), the Ounane pluton is located in a typical position for a potassic series while the Tisselliline (except R666) forms an alkaline trend. The sample R666 is far from the other samples due to a peculiar enrichment in Nb (52 ppm) and in Ta (4.9 ppm). This is coupled with low K_2O (Fig. 11A) and Ba contents but also to a high Rb/Sr (Fig. 10B), high Al_2O_3 and U content when compared to other Tisselliline granitoids (Table 1).

The rare earth elements from the Ounane pluton show classical spectra (Fig. 12A) for a K-rich series for light REE (LREE) but with a large set of heavy REE (HREE), La_N/Yb_N varying from 14 to 181. High La_N/Yb_N are reminiscent of Archaean granitoids (Martin, 1987).

The three samples from the Tisselliline pluton grouped in Fig. 11C have similar REE patterns with a strong LREE/HREE fractionation (Fig. 12B): La_N/Yb_N vary from 96 to 143, also reminiscent of Archaean granitoids. The sample R666, already noted for its peculiar chemistry, presents a seagull spectra with a nearly flat pattern and a strong negative anomaly ($Eu/Eu^* = 0.02$), typical of subsolidus re-equilibration with halogen-rich fluids, another characteristics of alkaline series. The sample R680 is very low in REE content ($\sum REE = 36$ ppm for 600–700 ppm for the main trend) and displays a positive Eu anomaly ($Eu/Eu^* = 2.49$), suggesting the presence of cumulative feldspar or that this granite is a low degree fluid-present partial melt of a felsic source (Harris and Inger, 1992).

The mean REE of the three Tisselliline samples from the main trend (R676, 678, 679) and the mean of the Ounane granitic samples (>72% SiO_2; Fig. 12C) are subparallel with the Tisselliline being more enriched than the Ounane, both marked by a strong LREE/HREE fractionation.

The Ounane pluton displays MORB-normalized spidergrams that are very close for most trace elements for rocks ranging from 63% to 73% SiO_2 (Fig. 12D). Only P and Ti display strong inverse correlations with SiO_2 (apatite and ilmenite or titanite role) and as already noted, Yb and Y are quite variable. LILE anomalies correlate with SiO_2: positive for K and Rb, negative for Sr and Ba. The plagioclase plays a major role either in

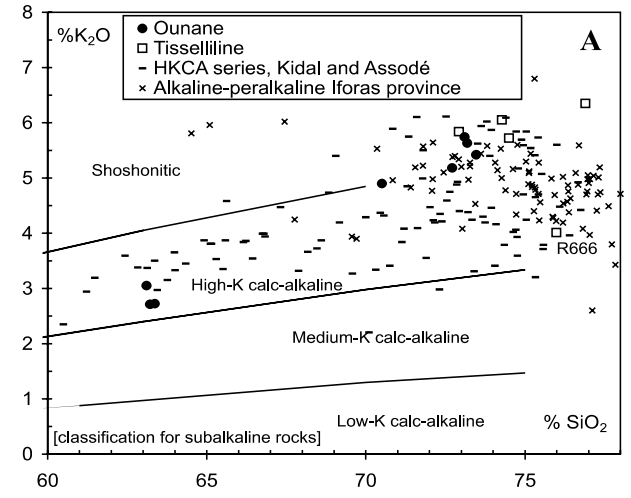

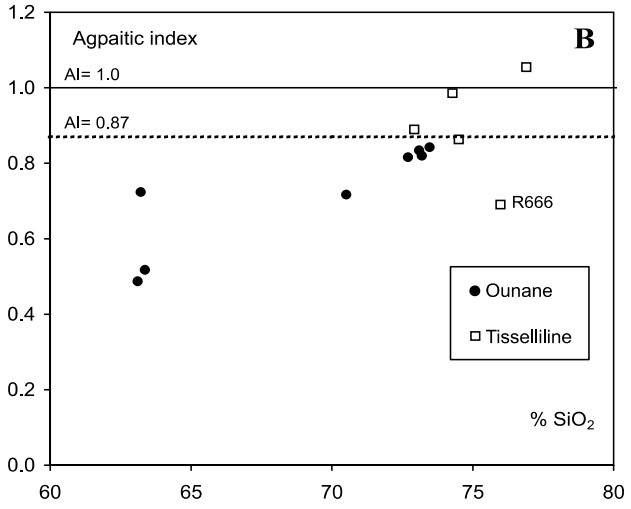

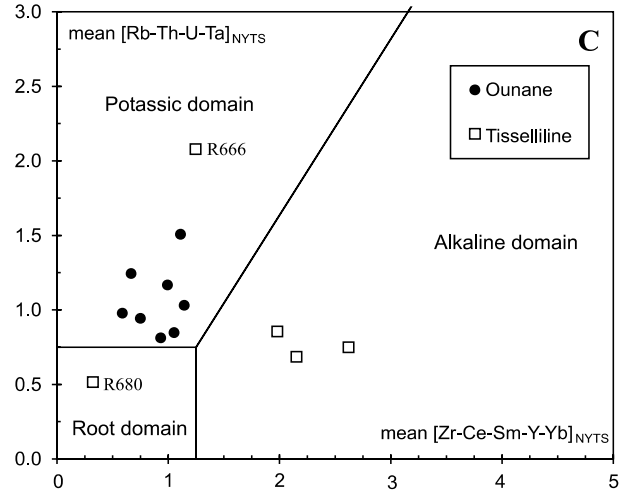

Fig. 11. Geochemistry of the Ounane and Tisselliline plutons: (A) SiO_2 vs. K_2O; (B) SiO_2 vs. agpaitic index ($[K_2O + Na_2O]/Al_2O_3$, in molar proportions); AI = 0.87 from Liégeois and Black (1987), separating the HKCA series from the alkaline–peralkaline series in the Kidal terrane; (C) synthetic diagram with sliding normalized values to the Yenchichi–Telabit reference series (Liégeois et al., 1998), see text.

the fractional crystallization or in the partial melting process. As a whole, the Ounane pattern (enrichment in LILE, Nb–Ta negative anomaly, low Y–Yb content and strong slope from Ce to Yb) indicates a subduction-related source (but not necessarily a subduction environment at the time of Ounane intrusion). The REE patterns are reminiscent of Archaean.

For the Tisselliline pluton, the MORB-normalized spidergrams (Fig. 12E) distinguishes the main trend (R676, 678, 679) from the two samples displaying particular REE patterns and sliding normalized values (R666 and 680). As for the REE, the main trend displays a pattern parallel to that of the Ounane pluton (Fig. 12F) but with higher values for LREE, MREE, Zr and Hf and lower values for Ba. These differences can be linked to the more alkaline character of the Tisselliline pluton. However a source similar to that of the Ounane is likely, with differences in fluid activity as marked by the sample R666 or in partial melting degree, as marked by the sample 680.

In conclusion, the geochemical data point to a high-K calc-alkaline series for the Ounane pluton and to an alkaline series for Tisselliline pluton but in both cases, the source possesses subduction-related characteristics and Archaean affinities. Let us note that this concerns the source of the studied pluton, and not their palaeoenvironments: the subduction-related geochemistry of the source could have been acquired a long time before the Ounane and Tisselliline emplacements. The Tisselliline pluton displays more variations than the Ounane pluton due to greater fluid activity and lower degree of partial melting or higher degree of crystal fractionation. To resolve these last points is out of the scope of this study.

4.3. Nd and Sr isotope geochemistry

The Rb–Sr isochron ages are taken as the intrusion age of the Ounane pluton (624 Ma) and for the Tisselliline pluton (555 Ma). Using individual initial ratios will integrate the error on the ages. Comparisons will be made with the gneissic country-rocks (Nd isotopes; Peucat et al., 2003, this issue), with the Anfeg pluton from the Laouni terrane that is in a similar context (Sr and Nd isotopes; Acef et al., 2003, this issue) and with the Renatt regional parautochthonous crustal leucogranite from the Assodé-Issalane terrane, just to the east (Figs. 1 and 2; Sr and Nd isotopes; Liégeois et al., 1994). This latter granite represents a lower granulitic crustal melt mixed at the intrusion level with an amphibolite-facies crustal melt at ≈666 Ma (Rb–Sr isochron; Liégeois et al., 1994).

A T_{DM} model age (calculated following Nelson and DePaolo, 1985) vs. ε_{Nd} diagram is opposing correlated

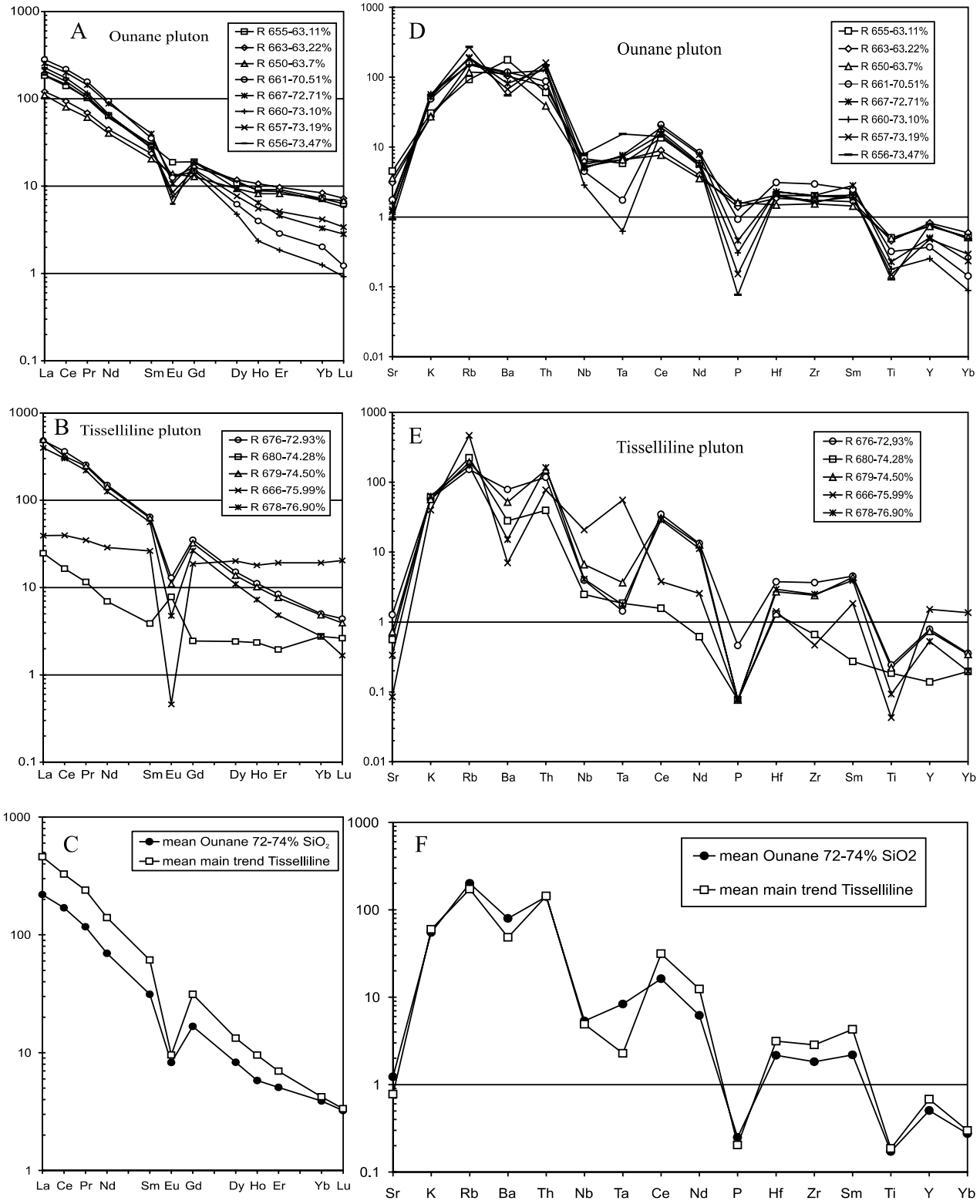

Fig. 12. Geochemistry of the Ounane and Tisselliline plutons: (A) REE diagram for the Ounane pluton; (B) REE diagram for the Tisselliline pluton; normalization to chondrite (Taylor and Mc Lennan, 1985); (C) means of the Ounane granites ($SiO_2 > 72\%$) and of the main trend of the Tisselliline pluton (samples R676, 678, 679); (D) trace elements normalized to N-MORB (Sun, 1980; Pearce, 1982) for the Ounane pluton; (E) trace elements normalized to MORB for the Tisselliline pluton; (F) trace elements normalized to MORB for means of the Ounane granites ($SiO_2 > 72\%$) and of the main trend of the Tisselliline pluton (samples R676, 678, 679). Value next to the sample number is the silica content of this sample.

values (both are linked to the measured $^{143}Nd/^{144}Nd$) but the first privileges in addition the Sm/Nd ratio and the second the intrusion age. This diagram is particularly useful to compare the above lithologies (Fig. 13A). The Ounane pluton has T_{DM} model ages varying between 1920 and 2540 Ma with a mean of 2141 ± 122 Ma implying low ε_{Nd} at 624 Ma, between −14 and −21 (mean: -17.3 ± 1.6). The Tisselliline pluton gives slightly younger Nd model ages with T_{DM} between 1820 and 2040 Ma (mean: 1900 ± 85 Ma) and ε_{Nd} between −12.7 and −14.7 (mean: -14.2 ± 0.8). The Ounane trend follows that of the Renatt granite. However, when combining ε_{Nd} and Sr_i (Fig. 13B), we can note that the high ε_{Nd} end-member (at −14) of the Renatt granite has high Sr_i (up to 0.780) at 624 Ma, which is not the case for the Ounane. In this diagram, only the low ε_{Nd} (−19 to −22) end-member of the Renatt granite is close to one end of the Ounane trend. This Renatt end-member has T_{DM} varying from 2200 to 3200 Ma.

Fig. 13B shows that the Ounane–Tisselliline plutons form a trend parallel to the *Y*-axis with a small variation in Sr_i (allowing for errors in the Rb–Sr isochrons) compared to larger variations in ε_{Nd}. This can be interpreted as the result of mixing between a melt extracted from an Archaean/Palaeoproterozoic granulitic crust and a melt generated within the mantle. The latter

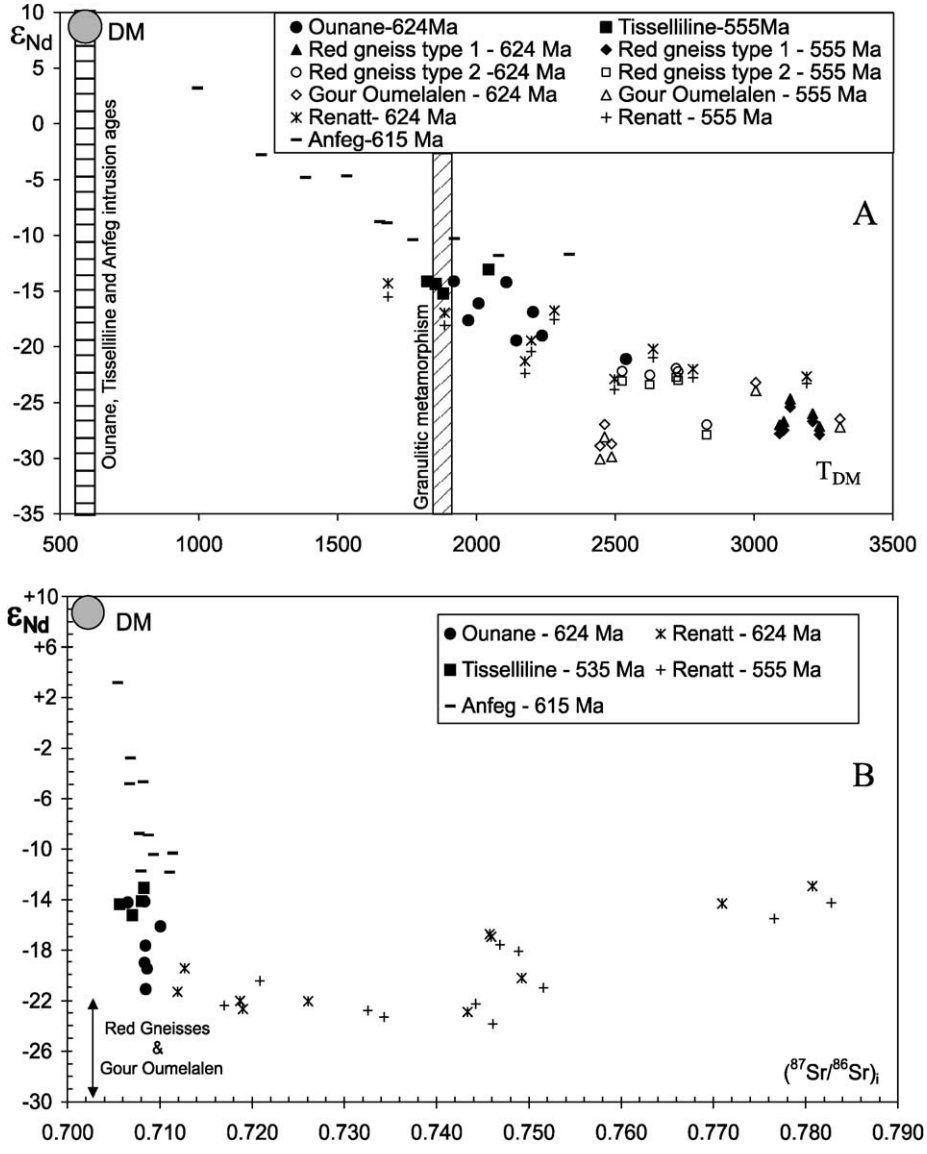

Fig. 13. Nd and Sr isotopes for the Ounane and Tisselliline plutons, compared with the Gour Oumelalen basement (Peucat et al., 2003, this issue), the Anfeg batholith from the Laouni terrane (Acef et al., 2003, this issue) and the parautochthonous Renatt leucogranite from the Assodé-Issalane terrane (Liégeois et al., 1994).

would be minor, particularly in the Ounane pluton. The Anfeg batholith (Laouni terrane; Acef et al., 2003, this issue) would have a greater juvenile input in its genesis (Fig. 13B). The older the melted crust is, greater the juvenile input has to be (Fig. 13A). With a larger juvenile input, the source of the Archaean Red gneiss complex (group 1) would be a suitable source for the Ounane and Tisselliline plutons. The difference observed in the geochemistry of the Ounane pluton vs. the Tisselliline pluton could be due to the mantle source involved in the process (Liégeois et al., 1998). This shows that alkaline–peralkaline granitoids can be rooted either mainly in the lower crust (Tisselliline) or in the mantle without crust contribution (Tin Zebane dyke swarm in Tassendjanet terrane; Fig. 1; Hadj Kaddour et al., 1998; Aït-Djafer et al., 2003, this issue).

5. Geodynamic implications—the LATEA metacraton

5.1. The evolution of the LATEA cratonic passive margin during Neoproterozoic time

The LATEA composite terrane (Fig. 14) is made of an Archaean (≈2.7 Ga with protolith up to 3.3 Ga; Peucat et al., 2003, this issue) and Palaeoproterozoic basement (2.1–1.9 Ga; Bertrand et al., 1986; Peucat et al., 2003, this issue); the Eburnian orogeny (≈2 Ga) produced a granulitic facies metamorphism.

No Mesoproterozoic event or rock is recorded in LATEA and in the entire Tuareg shield. This means that LATEA had plenty of time to acquire a thick lithospheric mantle (Black and Liégeois, 1993), rendering it very rigid, i.e. cratonic.

A model can be proposed for the Neoproterozoic evolution of LATEA (Fig. 15).

The remarkable thrust eclogitic unit that can be followed from the south to the north of LATEA (Figs. 1 and 2) can be used to estimate relative Pan-African displacements along the mega-shear zones. Indeed, this eclogitic unit constitutes a geological marker of the first order, not only to define the pre-collision and collision conditions but also to determine the post-collisional movements along the mega-shear zones. In this case, it shows minimum relative movements to the north of ≈500 km, probably much more in an absolute frame. This allows an initial configuration for LATEA to be suggested before the Pan-African orogeny at around 900 Ma ago, as forming one cratonic passive margin (Fig. 15A). The Iskel island arc was offshore with the subduction plane dipping away from LATEA.

At 870–850 Ma (age of the syn- to late-kinematic plutons (Caby et al., 1982) in the Iskel terrane), the LATEA continent entered the subduction zone east of the Iskel island arc, with the result that the Iskel terrane

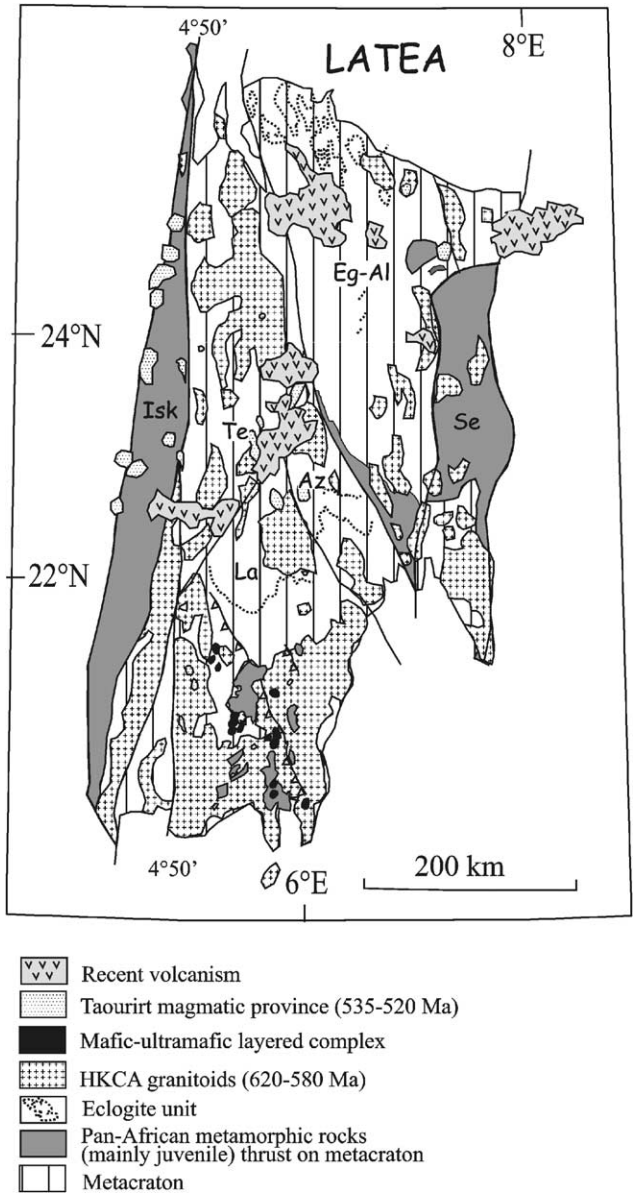

Fig. 14. Present situation of LATEA showing the preserved Archaean–Palaeoproterozoic basement (metacraton) dissected in four terranes (La = Laouni, Az = Azrou-n-Fad, Te = Tefedest, Eg-Al = Egéré-Aleksod), the thrust juvenile material (at ≈850 Ma [Isk = Iskel], ≈685 Ma and even probably later [Se = Serouenout]), the high-K calc-alkaline (HKCA) batholiths (620–580 Ma), the mantle-derived mafic–ultramafic layered complexes, the alkaline-alkali-calcic plutons (Taourirts) mainly localized on the western boundary of LATEA and the recent Tuareg volcanism mainly located in the LATEA metacraton (forming, with that located along the Saharan craton in Aïr, 95% of this volcanism in the Tuareg shield).

can be considered as the remnants of this arc lying upon the western margin of LATEA (Fig. 15B). This position on a cratonic margin has protected this thrust terrane from later events, as was the case for the Barghot and Aouzegueur terranes, thrust at 720–700 Ma onto the

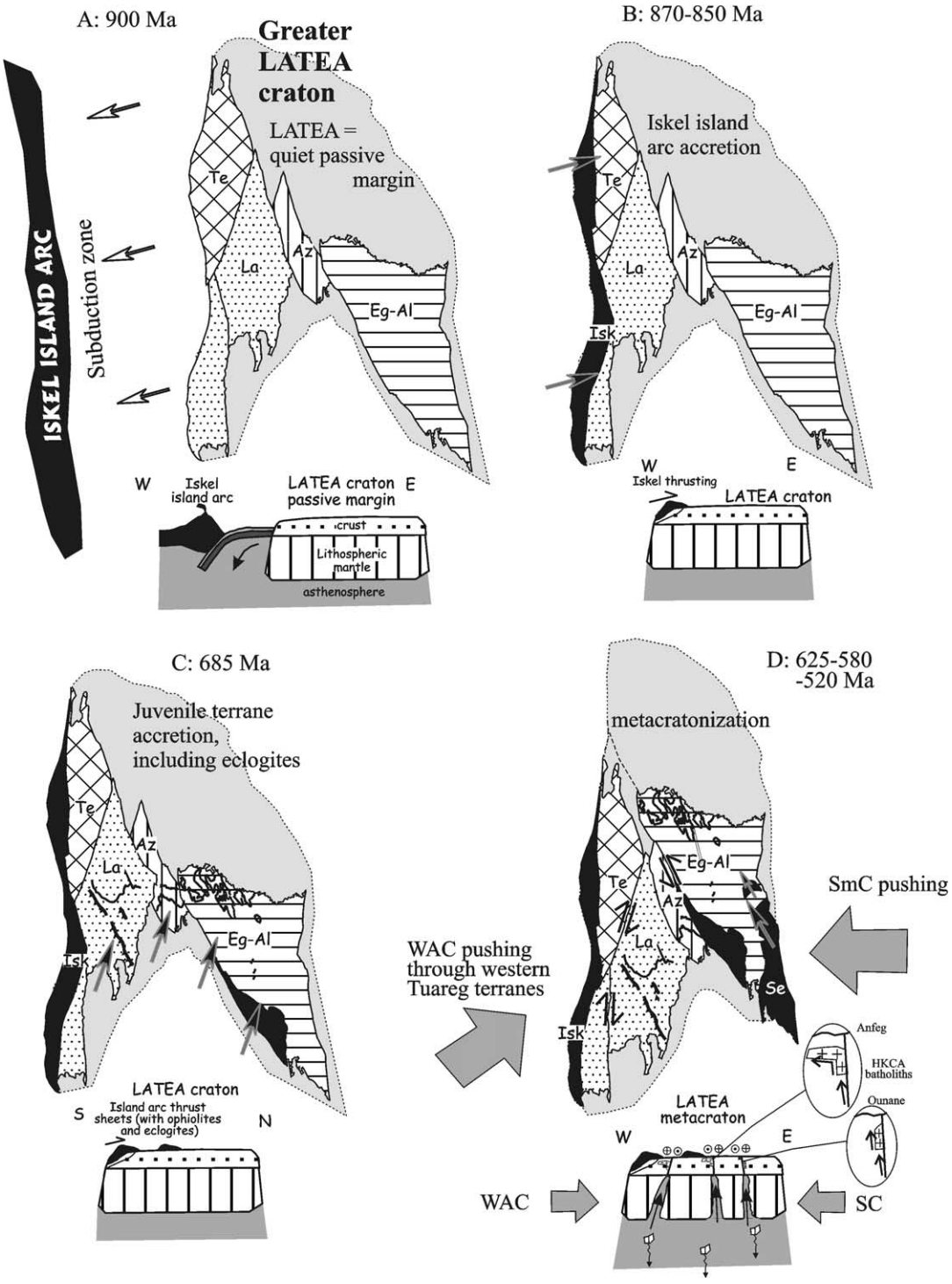

Fig. 15. Model reconstituting the LATEA behaviour during the Neoproterozoic, i.e. the evolution of LATEA from a craton to a metacraton. (A) ≈900 Ma: LATEA constitutes a passive margin without any applied stress; this is the period of the building of the Iskel island arc with the subduction plane dipping away from LATEA craton; the limits of the greater LATEA craton is inferred from available drillings (Latouche, pers. observations). (B) 870–850 Ma: accretion of the Iskel island arc onto the LATEA cratonic passive margin. (C) Accretion onto LATEA of juvenile terrains represented by eclogites, ophiolites and other various oceanic lithologies, including that studied here in the Tin Begane area. (D) Period of metacratonization of LATEA: LATEA is squeezed between the West African craton (WAC) to the east and the Saharan craton (SC) or metacraton (SmC) to the east. LATEA is dissected by mega-shear zones generating linear lithospheric delamination and asthenospheric uprise. This generated partial melting of the Archaean lower crust and the intrusion of HKCA batholiths (see Fig. 14) along these shear zones, expanding along subhorizontal structures (Anfeg-type) or not (Ounane-type); there are still maybe some juvenile oceanic terranes that accreted (Serouenout). Some parts of the Archaean–Palaeoproterozoic basement are uplifted or included into thrust sheets. At 555 ± 15 Ma, the Tisselliline high-level pluton intruded in a transpressional regime. At 530–520 Ma, there is the intrusion of the alkaline and alkali-calcic shallow level plutons in particular along the western

Saharan craton (Liégeois et al., 1994) for the same reason. This collision did not destabilize the LATEA craton.

At ≈685 Ma (Fig. 15C), another collision with a subduction zone took place: a series of thrusts of oceanic material occurred from SW to NE on the southern border of LATEA. This event destabilized locally the LATEA craton, as old basement rocks were introduced into the thrust sheets, but probably did not produce a regional destabilization. Such thrusts occurred probably also later as for the Serouenout terrane, thrust towards the NW (Fig. 15D).

The younger Neoproterozoic effects are transcurrent movements along subvertical shear zones accompanied by the intrusion of high-K calc-alkaline batholiths that expanded horizontally away from the shear zones (Latouche, 1975, 1978; Bertrand et al., 1986; Acef et al., 2003, this issue; Fig. 15D). Dated batholiths are within the 625–580 Ma age range (Bertrand et al., 1986; this study). Later transpressive movements at higher structural levels occurred at 555 ± 15 Ma (Tisselliline pluton, this study) and transtensive movements in the range 535–525 Ma (Sn–W enriched small plutons; Cheilletz et al., 1992; Taourirt plutons; Azzouni-Sekkal and Boissonnas, 1993; Bonin et al., 1998; Paquette et al., 1998; Azzouni-Sekkal et al., 2003, this issue). This corresponds to a widespread greenschist facies retrogression dated at 522 ± 27 Ma (this study).

Granitoids are not regularly disposed in LATEA: they are sparse in the Egéré-Aleksod terrane (Fig. 14) and abundant to the south in the Laouni terrane. In all cases, these batholiths are flat and thin in most of their surface, having a subvertical foliation only in the vicinity of the transcurrent mega-shear zone. The Ounane and Tisselliline plutons studied in the NE of the Egéré-Aleksod terrane are meaningful in this regard: being an extreme case, they strongly constrain the genesis of LATEA batholiths. Both are linked to an intra-terrane mega-shear zone, the Ounane as a middle crust intrusion, the Tisselliline as an upper crustal intrusion. Both show internal structures that agree with an emplacement within a transpressive context. Although being distinct geochemically (the Ounane is high-K calc-alkaline, the Tisselliline is alkaline), they share several major geochemical characteristics (Fig. 12C and F) and reflect melting of a Palaeoproterozoic–Archaean granulitic lower crust (giving rise to T_{DM} model ages between 1820 and 2540 Ma); this melting was generated by a mantle input that is seen by the Nd and Sr isotopes. The geochemical differences existing between the two plutons must then be probably searched within the mantle component.

This mixed crustal dominated source associated with mega-shear zones can be linked to the structure observed in current mega-shear zones, such as the Red River shear zone in Asia or the San Andreas Fault in California. In both cases, high heat flow indicates that the asthenospheric mantle is close to the Moho (Lachenbruch et al., 1985; Leloup and Kienast, 1993). In the case of the San Andreas shear zone, the lithospheric mantle is lacking (Lachenbruch et al., 1985). This suggests that a lithospheric delamination occurs along mega-shear zones, where the cold lithospheric mantle sinks and allows the hot asthenospheric mantle to reach the Moho (Fig. 15D). This generates mantle melts by adiabatic pressure release and crustal melts in the lower crust due to the high heat flow. Some mixing can occur between the mantle and the lower crustal melts. The resulting magmas will follow the shear zone and will intrude at different level in the crust. An intrusion in the mid crust can follow horizontal foliations at the discontinuity formed by the juvenile thrust sheets over the old basement (Anfeg-type; Acef et al., 2003, this issue). They can also stick to the mega-shear zone (Ounane-type), which will be the rule at higher structural levels (case of the Tisselliline and of the Taourirt plutons; Azzouni-Sekkal et al., 2003, this issue). To the south of LATEA, the phenomenon was more intense, resulting in abundant HKCA batholiths with a more important mantle component in their source (Anfeg-type; Acef et al., 2003, this issue). There are also intrusions of mantle-derived mafic–ultramafic layered complexes (Cottin et al., 1998; Fig. 14), variably contaminated by the Archaean lower crust. The Pan-African shear zones with thinner lithospheric mantle probably also played a role in the localization of the recent Hoggar volcanism (Fig. 14).

This dissection, accompanied by linear lithospheric delamination, occurred in a general transpressional system allowing an escape of the LATEA terranes to the north. This was accompanied by the reactivation and the uplift of the basement in the vicinity of the shear zones. In the region intruded by HKCA batholiths, a greenschist facies metamorphism was present at various degrees in both the basement and the early Pan-African thrust sheets. The closure of this retrograde phase has been dated here at 522 ± 27 Ma.

Fig. 15 (*continued*)
boundary of LATEA under a transtensional regime (Taourirt plutons; see Fig. 11). During the whole Pan-African orogeny, LATEA was not subjected to a major thickening, preserving a part of its rigidity; in turn, its Archaean–Palaeoproterozoic basement and the early Pan-African oceanic thrust sheets are well preserved.

5.2. The LATEA metacraton

The above story corresponds to the "hit and run" orogeny of Maxson and Tikoff (1996): the "hit" corresponds to early collisions marked by mega-thrusts and by high-pressure metamorphic rocks uplift and the "run" to large horizontal movements of terranes along subvertical mega-shear zones and accompanied by numerous granitoids, mainly high-K calc-alkaline in nature. This corresponds to the collisional and post-collisional periods as defined by Liégeois et al. (1998). However, in the LATEA case, the collision is not accompanied by a major crustal thickening and the Pan-African high-grade metamorphism is limited to the juvenile thrust sheets and to rare pieces of basement accompanying overthrusts. That means that the Archaean–Palaeoproterozoic basement is well preserved and that isotopic geochronometers, including the Rb–Sr geochronometer (Latouche and Vidal, 1974) applied to the basement rocks, generally did not record the Pan-African orogeny.

This intermediate character between a rigid, unaffected craton and a mobile belt completely affected by an orogeny corresponds to the notion of "metacraton" recently proposed by Abdelsalam et al. (2002). These authors defined a metacraton as a craton that has been remobilized during an orogenic event but that is still recognizable dominantly through its rheological, geochronological and isotopic characteristics. Indeed, LATEA behaved as a craton during the first part of the Pan-African orogeny but was partly destabilized and dissected during the second half, corresponding to the metacratonization process. In this case, the LATEA metacraton has preserved even Palaeoproterozoic petrological characteristics indicating that the metacratonization was of medium intensity.

This metacratonization occurred mainly during the 620–580 Ma period, but continued until 520 Ma (Fig. 15D). This is when the LATEA craton was squeezed between the nearly opposite pushing of the WAC and the SmC. This squeezing generated a general tectonic escape to the north of the Tuareg shield terranes. LATEA was not able to behave as one rigid body. It was dissected by mega-shear zones and intruded by HKCA batholiths and finally by shallow depth alkaline plutons (Fig. 15D).

The western boundary of LATEA is well marked by the 4°50′ fault with a western deviation to the south (Fig. 14). This fault dissected the Laouni terrane in two parts and generated spectacular cold mylonites (Lelubre, 1952). To the west, the In Teidini terrane is one of the terranes from the so-called "Pharusian belt" made up of juvenile lithologies and probably accreted to LATEA at the beginning of northward tectonic escape. The Archaean–Palaeoproterozoic terrane of In Ouzzal, located further west (Fig. 1) cannot have been a part of LATEA. This is confirmed by the age of the high temperature granulitic metamorphism (Ouzegane and Boumaza, 1996) that is 100 Ma older than in LATEA and by a more complex history as a whole (Peucat et al., 2003, this issue).

The eastern boundary of LATEA is less certain. The Tin Begane island arc thrusting occurred at 685 ± 19 Ma when that of Barghot–Aouzegueur terranes (Fig. 1) onto the Saharan metacraton was nearly finished and when the Assodé-Issalane terrane underwent post-collisional collapse (Liégeois et al., 1994). Relations between LATEA and the Assodé-Issalane terrane (Fig. 1) still have to be deciphered: gently dipping fuchsite-bearing quartzites that lie above high-grade gneisses in the north of Assodé-Issalane suggest a correlation with the same quartzites in the Gour Oumelalen Supergroup (Fabriès and Latouche, 1973) and along the western part of the Laouni terrane. However, the Assodé-Issalane terrane has been pervasively affected by a regional anatectic event resulting from collision with the Saharan metacraton (Renatt parautochthonous granite; Liégeois et al., 1994). The Assodé-Issalane terrane could then represent the eastern border of LATEA that collided with the Saharan craton at ≈700 Ma or could be a distinct microcontinent. A general problem that has still to be deciphered is the relation existing between LATEA and Saharan metacratons: is LATEA the western extension of the Saharan metacraton?

6. Conclusions

The Central Hoggar is made of four terranes (Laouni, Azrou-n-Fad, Tefedest and Egéré-Aleksod) grouped under the acronym LATEA as they share major characteristics.

(1) Their basement is made of granulitic facies rocks metamorphosed during the Eburnian orogeny (≈1.9 Ga; Bertrand et al., 1986; Peucat et al., 2003, this issue); the protoliths are either Palaeoproterozoic or Archaean (up to 2.7 Ga, zircon ages, or 3.3 Ga, T_{DM} Nd model ages; Peucat et al., 2003, this issue).

(2) No Mesoproterozoic rocks or events are known.

(3) Neoproterozoic rocks are juvenile oceanic units lying upon the old granulitic basement. They range from greenschist facies ophiolites to garnet amphibolites and gneiss and eclogites giving a complete retrogressive *P–T–t* path from >15 kbar—790 °C to 4 kbar—500 °C through 12 kbar—830 °C and 8 kbar—700 °C. These island arc rocks have been metamorphosed in a subduction zone and afterwards thrust during early Pan-

African phases from ≈850 Ma (Iskel terrane; Caby et al., 1982) to 685 ± 19 Ma (Laouni thrust sheets) and even probably later (Serouenout terrane). LATEA has not been intruded by subduction-related magmas during this period; LATEA behaved as a passive margin. The early thrusts are remarkably preserved, as is the old basement, if shear zones are ignored. This indicates that the LATEA passive margin was rigid, i.e. cratonic, during these early Pan-African phases of accretion.

(4) The late Pan-African phase is marked by the collision with the West African craton to the west, inducing a general tectonic escape of the Tuareg terranes to the north (Black et al., 1994). During this period, LATEA was squeezed between the West African craton to the west (through the western Tuareg terranes) and the Saharan metacraton to the east (through a fringe of eastern terranes; Liégeois et al., 1994). This resulted in the dissection of LATEA into four terranes by mega-shear zones that induced relative movements of several hundred kilometres. This transpressive major tectonic phase induced the emplacement of high-K calc-alkaline batholiths along the shear zones with some of them expanding horizontally along older thrust planes. To the north, where they are few, their source is mostly the Archaean basement at depth with only a small mantle input (Ounane pluton, 624 ± 15 Ma; $\varepsilon_{Nd} = -17.3 \pm 1.6$). To the south, where they are numerous, the mantle input is more important, even with mantle-derived mafic–ultramafic layered complexes (Cottin et al., 1998). In our model, we relate this to a linear lithospheric delamination along the mega-shear zones allowing the hot asthenosphere to rise, melt by adiabatic pressure release and melt the lower crust. These linear delaminations left intact large areas between the shear zones. At the end of this phase, high-level circular plutons intruded along these shear zones, first during transpression (Tisselliline pluton, 555 ± 15 Ma; $\varepsilon_{Nd} = -14.2 \pm 0.8$), afterwards during trans-tension (Taourirt plutons; Azzouni-Sekkal et al., 2003, this issue).

This dismembered and partly destabilized the LATEA craton. This corresponds to a metacratonization process that, if completed, would have led to a mobile belt comprising old protoliths. It may be for LATEA that this process was only incipient, leaving most of LATEA and its thrust superstructures nearly intact. This matches the notion of metacraton (Abdelsalam et al., 2002). The LATEA metacraton, in the centre of the Pan-African belt, constitutes a museum for middle Neoproterozoic, Palaeoproterozoic and Archaean events.

LATEA formed during the Eburnian orogeny, grew as a craton during the Mesoproterozoic by acquiring a thick lithospheric mantle (Black and Liégeois, 1993), a rigidity allowing the preservation of early Pan-African events, and finally became a metacraton during the final amalgamation of the Trans-Saharan belt.

Acknowledgements

We would like to dedicate this work to Russell Black with whom we initiated the terrane concept in the Tuareg shield during fascinating periods of discussion, of work and of writing. Lively discussions with R. Caby were appreciated. R.J. Stern and O. Eklund are warmly thanked for their constructive reviews. We express gratitude to J. Boissonnas and R.J. Stern for help with the English. This work is a contribution to project ''Héritage éburnéen et structuration panafricaine du Hoggar: étude géologique et géophysique'' supported by the French–Algerian cooperation program 00MDU476. This is a contribution to 1GCP485 and to NATO project EST/CLG 979766.

Appendix A. Analytical techniques

Electron microprobe analysis (University of Paris 6 and M.N.H.N): The minerals have been analysed using a Camebax electron microprobe. The operating conditions were 15 kV and 10 nA, with a counting time of 20 s, except for volatile elements in biotite and plagioclase. Natural silicates and synthetic oxides were used as reference for all elements. For details, see Mouri et al. (1996).

Whole-rock major and trace elements (Africa Museum): Si, Al, Ti, Fe, Ca and P have been analyzed by X-ray fluorescence following the method described by Norrish and Hutton (1969); Mn, Mg, K and Na have been measured by atomic absorption after open acid digestion ($HF + HClO_4 + HNO_3$); FeO has been titrated by $KMnO_4$. Three different techniques have been used for the analysis of 29 trace elements: X-ray fluorescence on raw material for Rb and Sr; ICP-AES for Cu, Zn, Cr and Co (for details, cf. Navez, 1983); ICP-MS (VG PQ2+) for the other elements: the result of the alkaline fusion (0.3 g of sample + 0.9 g of lithium metaborate at 1000 °C during 1 h) has been dissolved in 5% HNO_3. The calibrations were set using both synthetic solution (mixture of the considered elements at 2, 5 and 10 ppb) and international rock standards (BHVO-1, W1, GA, ACE). For all these elements, the precision varies from 5% to 10% (for details, see Navez, 1995).

Rb–Sr and Sm–Nd geochronology (Africa Museum): After acid dissolution of the sample and Sr and/or Nd separation on ion-exchange resin, Sr isotopic compositions have been measured on Ta simple filament (VG Sector 54), Nd isotopic compositions on triple

Ta–Re–Ta filament (VG Sector 54) and Nd concentrations (isotope dilution) on Re double filaments (Finnigan MAT 260). Repeated measurements of Sr and Nd standards have shown that between-run error is better than 0.000015 (2σ). The NBS987 standard has given a value for $^{87}Sr/^{86}Sr$ of 0.710275 ± 0.000006 (2σ on the mean, normalized to $^{86}Sr/^{88}Sr = 0.1194$) and the MERCK Nd standard a value for $^{143}Nd/^{144}Nd$ of 0.511730 ± 0.000010 (2σ on the mean, normalized to $^{146}Nd/^{144}Nd = 0.7219$) during the course of this study. All measured ratios have been normalized to the recommended values of 0.710250 for NBS987 and 0.511963 for Nd Merck standard (corresponding to a La Jolla value of 0.511858) based on the 4 standards measured on each turret together with 16 samples. Sm and Nd concentrations were measured by isotope dilution. The error on the Sm/Nd ratio is ~2%. The Rb–Sr and Sm–Nd ages have been calculated following Ludwig (1999). Decay constant for ^{87}Rb (1.42×10^{-11} a^{-1}) was taken from Steiger and Jäger (1977) and for ^{147}Sm (6.54×10^{-12} a^{-1}) from Lugmair and Marti (1978). Sr and Nd isotope ratios are listed in Tables 2 and 3.

Laser ablation ICP-MS (Africa Museum): The data listed in Table 4 were obtained on a Fisons PQ2+ Plasma Quad coupled to a Fisons Laserprobe. General working conditions were:

- Plasma conditions: RF Power: 1.35 KW Forward, <3 W reflected; Glas flow rates: Ar Cool gas flow (13.5 $l min^{-1}$); Ar Auxiliary gas flow (1.15 $l min^{-1}$); Ar Nebulizer gas flow: (0.9 $l min^{-1}$).
- Interface: Sampling cone (Ni 1.0 mm aperture), Skimmer cone: (Ni 0.7 mm aperture).
- Laser system (Spectrum SL282 Nd:YAG): Laser beam: (IR; wavelength: 1065 nm); operating mode (Q-switchted); energy (280 mJ/pulse); repetition rate (10 Hz); pre-ablation time (7 s/shot); acquisition time (15 s); crater size (50 μm).
- Acquisition parameters: detector type (Galileo channeltron); ion detection (pulse counting; mode: peak jumping with 3 pts/peak; dwell time: 10.24 ms; DAC/step: 5.

Rock samples were prepared as thin sections whose thicknesses were set to 150–200 μm. This thickness range still allows recognizing minerals under the polarizing microscope.

The quality of the data depends on calibration, interference correction and drift control. In addition, there is the reproducibility of the laser ablation. The latter and the drift are largely controlled by the knowledge of the concentration of an element used as internal standard. We chose here a major element, Ca, which has been measured close to each laser spot by electron microprobe. Interferences are well-known and corrected in consequence:

Element	m/z	Interferences
Eu	151	$^{135}Ba^{16}O$; $^{134}Ba^{16}OH$
Dy	163	$^{147}Sm^{16}O$
Gd	157	$^{141}Pr^{16}O$; $^{140}Ce^{16}OH$
Sm	152	$^{135}Ba^{16}OH$
Er	166	$^{150}Nd^{16}O$; $^{150}Sm^{16}O$
Yb	172	$^{156}Gd^{16}O$; $^{156}Dy^{16}O$
Hf	178	$^{162}Dy^{16}O$; $^{162}Er^{16}O$
Ta	181	$^{165}Ho^{16}O$

These interferences are quite low in this case, as Ba, the main interferent, is low in garnet and in clinopyroxene.

The calibration problem is delicate for laser ablation analysis particularly for infrared laser, more sensitive to matrix variability. In our case, it was crucial to use external standards with composition and concentration close to analysed samples. As natural international reference of garnet and pyroxene are lacking, we used a home garnet and pyroxene standard. The latter were selected for homogeneity (verified by laser ablation) and their bulk composition was measured into solution by ICP-MS (high-pressure acid digestion on three fractions from the same crystal). The concentrations in mg/l of these home standards are:

Element	Diopside	Garnet
Sc	57	42
Co	16.3	75
G	1.1	11.0
Ge	3.1	2.5
Sr	2030	0.9
Zr	5.6	73
Ba	3.6	0.8
Hf	0.24	1.3
Pb	1.4	<0.2
La	6.7	<0.2
Ce	18.8	0.3
Pr	2.9	<0.2
Nd	14.0	1.56
Sm	3.0	1.8
Eu	0.86	1.14
Gd	2.3	5.0
Dy	1.1	9.9
Er	0.35	6.2
Yb	0.27	5.1

Relative errors are estimated to be around 10%.

For elements such as Ti, V, Cr, Ni, Rb, Nb, Ta, W, Th and U, concentrations in these natural home standards are too low to be used as reference and we used instead NIST 610 and NIST 620 artificial glasses (international standards).

Table 4
Laser ablation ICP-MS trace elements of garnet and clinopyroxene

Sample	Sc	Ti	V	Cr	Co	Ni	Ga	Ge	Rb	Sr	Zr	Nb	Ba	La	Ce	Pr	Nd	Sm	Eu	Gd	Dy	Er	Yb	Hf	Ta	W	Pb	Th	U
Mean garnet 675-TB																													
c1-a (15 pts)	61	130	54	11	35	13	6	5	0.09	0.6	5.0	0.2	2.8	0.07	0.11	0.04	0.18	0.14	0.20	2.07	8.9	21.6	39.9	0.23	0.03	0.21	0.14	0.24	0.09
c1-b (14 pts)	59	149	67	26	40	11	8	7	0.06	2.3	4.5	0.1	40	0.06	0.09	0.03	0.16	0.22	0.14	1.82	8.7	19.7	36.3	0.20	0.06	0.16	0.18	0.17	0.03
c2-a (6 pts)	48	133	71	28	32	15	6	4	0.10	3.1	6.6	0.2	10	0.04	0.18	0.06	0.12	0.15	0.13	2.45	8.1	16.4	26.7	0.32	0.05	0.37	0.23	0.25	0.14
c2-b (6 pts)	58	121	67	22	36	19	7	5	0.11	0.8	4.4	0.1	1.4	0.11	0.20	0.05	0.15	0.17	0.17	1.81	8.6	17.3	27.0	0.19	0.09	0.22	0.30	0.39	0.11
c2-c (6 pts)	52	110	57	10	34	17	7	7	0.10	0.6	3.5	0.1	0.5	0.08	0.20	0.05	0.54	0.25	0.25	2.59	8.6	11.5	15.7	0.23	0.01	0.25	0.14	0.22	0.12
c2-d (3 pts)	56	88	53	6	32	17	7	7	0.10	1.0	2.6	0.1	0.8	0.06	0.22	0.05	0.18	0.13	0.13	2.16	8.2	10.9	13.9	0.16	0.00	0.18	0.25	0.32	0.09
Mean garnet 680-2																													
c1-a (5 pts)	53	443	124	12	39	22	9	4	0.18	2.2	157	0.3	44	0.10	0.60	0.17	0.59	0.43	0.23	2.65	10.5	18.8	26.2	2.99	0.10	0.33	0.28	0.33	0.29
c1-b (1 pt)	49	1377	156	16	39	26	8	4	0.12	13.4	108	3.2	2.9	9.7	23.4	3.1	16.1	4.9	1.4	6.1	12.9	12.2	9.9	2.2	0.2	1.9	1.0	6.2	1.0
c2-a (3 pts)	53	624	157	14	41	27	9	4	0.10	1.4	150	0.2	21	0.28	0.66	0.07	0.57	0.51	0.38	4.10	14.5	19.7	17.4	2.43	0.14	0.25	0.43	0.60	0.02
c2-b (3 pts)	75	256	102	16	35	113	12	6	2.32	117	615	1.2	157	1.3	1.8	0.5	3.9	1.5	1.1	3.4	6.7	4.4	4.1	10.6	0.4	1.0	2.0	1.8	0.9
c2-c (1 pt)	35	829	177	11	53	13	11	4	0.12	15.0	508	0.2	31	3.3	8.1	1.0	4.4	1.1	0.5	3.9	17.9	25.8	21.7	7.6	0.0	0.0	0.9	1.6	0.5
Mean garnet 648-3																													
c1-a (4 pts)	55	1361	153	33	42	26	11	7	0.25	2.4	48	2.9	77	0.25	0.38	0.10	0.65	0.21	0.37	4.97	28.1	34.8	37.7	1.18	0.21	1.17	1.37	0.18	0.37
c1-b (10 pts)	30	1243	93	20	32	28	12	4	1.02	27.3	228	2.3	352	0.37	1.22	0.16	0.99	0.68	0.84	4.69	5.33	1.84	1.19	3.18	0.23	0.54	1.71	0.33	0.42
c1-c (7 pts)	37	6689	105	32	34	24	11	5	0.36	7.2	268	13	75	2.4	8.7	1.4	8.9	3.5	2.0	11.8	15.4	6.8	4.3	3.4	1.4	1.4	0.8	0.8	2.6
c1-d (1 pt)	38	384	102	15	36	39	13	7	0.21	8.4	10.7	0.7	1	42	84	10	49	6.6	2.3	13	11	3.42	1.69	0.45	0.08	0.87	1.4	9.5	2.0
c2-a (10 pts)	53	1297	167	44	38	35	11	9	0.39	8.3	4.6	30	89	0.24	0.37	0.09	0.75	0.63	0.70	5.76	23.1	28.6	27.4	0.30	1.37	6.78	0.64	0.34	0.23
c2-b (2 pts)	61	678	157	45	49	37	12	7	0.19	2.4	4.0	10	5	0.23	0.35	0.05	1.09	0.85	0.81	8.46	15.2	6.59	4.01	0.41	0.47	3.10	0.82	0.18	0.13
c2-c (2 pts)	61	1758	188	50	52	51	14	11	0.57	5.3	6.4	3.5	50	2.6	9.7	1.4	7.5	2.6	1.3	8.8	20.7	28.4	24.8	0.7	0.4	2.6	1.6	1.0	3.1
Mean garnet 648-2																													
c1-a (15 pts)	59	168	71	111	17	1.1	6	4	0.63	0.6	33	0.1	0.3	0.09	0.22	0.03	0.28	1.31	0.18	6.65	26.9	26.7	23.1	1.20	0.04	0.20	0.13	0.11	0.23
c1-b (3 pts)	53	327	85	154	16	0.0	6	5	0.09	0.6	20	1.4	0.1	1.41	5.34	0.48	1.57	1.33	0.15	7.13	17.3	9.17	6.16	0.23	0.08	0.89	0.12	0.46	0.27
c1-c (1 pt)	77	501	107	197	23	0.4	9	8	0.34	0.7	461	1.2	0.5	25	61	7	24	6.9	0.9	13	17	19	17	6.9	0.13	0.27	0.66	17	8
c1-d (2 pts)	60	256	115	196	21	0.0	11	7	0.39	18.7	180	0.5	2.9	76	194	26	97	28	2.6	24	16	17	19	3.3	0.06	0.00	1.2	30	11
c2-e (9 pts)	44	150	42	72	15	0.9	4	3	0.35	0.4	11	0.7	0.1	0.10	0.12	0.11	0.36	0.82	0.08	5.46	22.5	20.1	15.3	0.45	0.16	0.20	0.22	0.15	0.17
Mean garnet 661-1																													
c1 (9 pts)	45	321	219	27	27	15	11	3	1.54	38.6	27	0.3	0.5	0.25	0.33	0.12	0.80	1.90	1.13	4.62	9.40	7.08	6.82	0.76	0.12	0.26	0.54	0.37	0.15
c2 (6 pts)	45	311	149	34	30	22	7	2	1.61	0.8	7	0.6	0.6	0.28	0.34	0.23	0.83	1.81	0.99	4.56	8.55	7.90	7.47	0.75	0.18	0.22	0.38	0.50	0.27
c3 (10 pts)	42	337	172	57	30	23	8	3	2.28	1.1	6	0.4	0.6	0.32	0.35	0.14	1.15	1.66	1.00	4.54	9.14	7.28	6.65	0.77	0.17	0.45	0.42	0.40	0.26
c4 (11 pts)	44	317	132	27	30	27	7	2	1.58	6.6	7	0.3	0.3	0.32	0.48	0.14	1.25	1.62	1.04	4.73	10.4	8.48	7.68	0.54	0.33	0.42	0.35	0.46	0.27
c5 (7 pts)	42	530	153	36	36	23	9	2	1.36	77.5	9	0.3	0.5	0.36	1.31	0.23	1.73	1.58	0.94	3.86	6.61	5.67	5.54	0.55	0.07	0.54	0.70	0.32	0.07
c6 (4 pts)	41	319	233	47	26	9	11	3	0.96	42.6	5	0.2	0.9	0.16	0.40	0.05	0.86	1.78	1.08	4.46	8.91	7.23	6.98	0.47	0.13	0.00	0.43	0.24	0.00
Mean clinopyroxene in single crystal																													
661-1cpx c6 (9 pts)	51	2764	725	59	46	80	18	2	1.00	161	31	0.4	4	1.06	5.02	1.14	7.22	3.42	1.32	4.33	4.74	2.23	1.15	1.31	0.02	0.56	1.00	0.21	0.05
661-1cpx c7 (5 pts)	44	1744	372	54	49	94	14	2	1.43	123	24	0.4	0.8	0.99	3.34	0.73	3.96	2.14	0.51	1.31	2.13	1.38	0.83	1.61	0.17	0.47	0.94	0.49	0.19
661-1cpx c8 (6 pts)	41	1921	449	67	53	100	14	2	0.96	56	24	0.2	1.1	0.76	3.55	0.75	3.85	1.84	0.48	1.89	1.68	0.98	0.65	1.17	0.15	0.16	0.65	0.38	0.18
Mean symplectite																													
661-1sym c1 (9 pts)	30	447	197	41	18	21	21	3	0.66	791	8	0.1	4	0.63	2.15	0.41	2.30	1.18	1.86	1.64	1.62	0.86	0.60	0.57	0.04	0.00	2.53	0.25	0.00
661-1sym c2 (12 pts)	34	563	196	30	17	26	23	3	1.06	821	52	0.2	8	0.71	1.98	0.40	2.79	1.71	2.04	1.89	2.25	0.95	0.59	1.57	0.08	0.22	2.23	0.30	0.08

Table 4 (*continued*)

Sample	Sc	Ti	V	Cr	Co	Ni	Ga	Ge	Rb	Sr	Zr	Nb	Ba	La	Ce	Pr	Nd	Sm	Eu	Gd	Dy	Er	Yb	Hf	Ta	W	Pb	Th	U
661-1sym c3 (11 pts)	25	904	158	54	15	28	16	2	0.80	689	7	0.4	5	0.62	2.01	0.42	2.72	2.00	1.61	2.18	2.39	1.21	0.81	0.63	0.07	0.22	2.12	0.23	0.11
661-1sym c4 (11 pts)	30	391	140	33	16	32	17	2	1.22	867	9	0.3	4	1.12	3.49	0.53	3.18	1.91	1.63	2.35	2.43	1.14	0.89	0.57	0.09	0.27	3.12	0.42	0.07
661-1cpx c3 (1 pt)	13	45312	179	33	7	11	16	2	0.26	651	45	29	3.47	2.88	18	4.56	25	15	4.20	20	21	8.56	4.09	2.11	2.20	1.15	2.23	0.55	1.01
648-3cpx (1 pt)	36	3898	322	52	55	60	28	4	5.07	57	20	6.2	713	2.04	11	2.38	15	5.01	2.50	6.96	6.07	1.48	1.67	0.82	0.28	0.49	5.78	0.18	0.67
648-3sym (6 pts)	33	426	86	27	34	58	39	5	16.9	172	35	3.0	1488	1.34	4.46	0.43	1.68	0.64	1.96	1.87	2.81	1.70	1.01	0.90	0.33	1.02	9.59	0.44	0.38

References

Abdelsalam, M., Liégeois, J.P., Stern, R.J., 2002. The Saharan metacraton. Journal of African Earth Science 34, 119–136.

Acef, K., Liégeois, J.P., Ouabadi, A., Latouche, L., 2003. The Anfeg post-collisional Pan-African high-K calc-alkaline batholith (Hoggar, Algeria), emplaced within the LATEA metacraton. Journal of African Earth Science, this issue.

Aït-Djafer, S., Ouzegane, K., Liégeois, J.P., Kienast, J.R., 2003. An example of post-collisional mafic magmatism: the gabbro-anorthosite layered complex from the Tin Zebane area (western Hoggar, Algeria). Journal of African Earth Science, this issue.

Azzouni-Sekkal, A., Boissonnas, J., 1993. Une province magmatique de transition du calco-alcalin à l'alcalin: les granitoïdes panafricains à structure annulaire de la chaîne pharusienne du Hoggar (Algérie). Bulletin de la Société Géologique de France 164, 597–608.

Azzouni-Sekkal, A., Liégeois, J.P., Bechiri-Benmerzoug, F., Belaidi-Zinet, S., Bonin, B., 2003. The "Taourirt" magmatic province, a marker of the very end of the Pan-African orogeny in the Tuareg Shield: review of the available data and Sr–Nd isotope evidence. Journal of African Earth Science, this issue.

Barbey, P., Bertrand, J.M., Angoua, S., Dautel, D., 1989. Petrology and U/Pb geochronology of the Telohat migmatites, Aleksod, Central Hoggar, Algeria. Contributions to Mineralogy and Petrology 101, 207–219.

Bertrand, J.M.L., Caby, R., 1978. Geodynamic evolution of the Pan-African orogenic belt: a new interpretation of the Hoggar shield (Algerian Sahara). Geologishe Rundschau 67, 357–388.

Bertrand, J.M.L., Caby, R., Lancelot, J.R., Moussine-Pouchkine, A., Saadallah, A., 1978. The late Pan-African intracontinental linear fold belt of the eastern Hoggar (central Sahara, Algeria): geology, structural development, U–Pb geochronology, tectonic implications for the Tuareg shield. Precambrian Research 7, 349–376.

Bertrand, J.M., Michard, A., Boullier, A.M., Dautel, D., 1986. Structure and U/Pb geochronology of Central Hoggar (Algeria): a reappraisal of its Pan-African evolution. Tectonics 5, 955–972.

Black, R., Liégeois, J.-P., 1993. Cratons, mobile belts, alkaline rocks and continental lithospheric mantle: the Pan-African testimony. Journal of Geological Society London 150, 89–98.

Black, R., Latouche, L., Liégeois, J.P., Caby, R., Bertrand, J.M., 1994. Pan-African displaced terranes in the Tuareg shield (central Sahara). Geology 22, 641–644.

Boissonnas, J., 1974. Les granites à structures concentriques et quelques autres granites tardifs de la chaîne pan-africaine en Ahaggar (Sahara central, Algérie). Thèse d'Etat, Centre de Recherches sur les zones arides, Série Géologie, 16, 662 p.

Bonin, B., Azzouni-Sekkal, A., Bussy, B., Ferrag, S., 1998. Alkali-calcic and alkaline post-orogenic (PO) granite magmatism: petrologic constraint and geodynamic settings. Lithos 45, 45–70.

Boullier, A.M., 1991. The Pan-African Trans-Saharan belt in the Hoggar shield (Algeria, Mali, Niger): a review. In: Dallmeyer, R.D., Lécorché, J.P. (Eds.), The West African orogens and circum-Atlantic correlatives. Springer-Verlag, Berlin, pp. 85–105.

Caby, R., Andreopoulos-Renaud, U., Gravelle, M., 1982. Cadre géologique et géochronologique U/Pb sur zircon des batholites précoces dans le segment pan-africain du Hoggar central (Algérie). Bulletin de la Société Géologique de France 24, 677–684.

Cheilletz, A., Bertrand, J.M., Charoy, B., Moulahoum, O., Bouabsa, L., Farrar, E., Zimmerman, J.L., Dautel, D., Archibald, D.A., Boullier, A.M., 1992. Géochimie et géochronologie Rb–Sr, K–Ar et ^{39}Ar–^{40}Ar des complexes granitiques pan-africains de la région de Tamanrasset (Algérie): relations avec les minéralisations Sn–W associées et l'évolution tectonique du Hoggar central. Bulletin de la Société Géologique de France 163, 733–750.

Cottin, J.Y., Guiraud, M., Lorand, J.P., 1990. Le magmatisme et le métamorphisme pan-africain témoins d'amincissement crustal dans la région de Laouni (Hoggar central, Algérie)? Comptes Rendus de l'Académie des Sciences Paris 311, 1345–1351.

Cottin, J.Y., Lorand, J.P., Agrinier, P., Bodinier, J.L., Liégeois, J.P., 1998. Isotopic (O, Sr, Nd) and trace element geochemistry of the Laouni layered intrusions (Pan-African belt, Hoggar, Algeria): evidence for post-collisional tholeiitic magmas variably contaminated by continental crust. Lithos 45, 197–222.

Djouadi, M.T., Ferré, E., Gleizes, G., Caby, R., Lesquer, A., Bouchez, J.L., 1997. Oblique magmatic structures of two epizonal granite plutons, Hoggar, Algeria: late orogenic emplacement of transcurrent orogen. Tectonophysics 279, 350–374.

Fabriès, J., Latouche, L., 1973. Présence de fuchsite dans les quartzites de la série charnockitique des Gour Oumelalen (Nord-Est de l'Ahaggar, Algérie). Bulletin de la Société Française Minéralogie et de Cristallographie 96, 148–149.

Guiraud, M., Powell, R., Cottin, J.Y., 1996. Hydration of orthopyroxene-cordierite-bearing assemblages at Laouni, Central Hoggar, Algeria. Journal of Metamorphic Geology 14, 467–476.

Hadj Kaddour, Z., Demaiffe, D., Liégeois, J.P., Caby, R., 1998. The alkaline–peralkaline granitic post-collisional Tin Zebane dyke swarm (Pan-African Tuareg shield, Algeria): prevalent mantle signature and late agpaitic differentiation. Lithos 45, 223–243.

Harris, N.B.W., Inger, S., 1992. Trace element modelling of pelite-derived granites. Contributions to Mineralogy and Petrology 110, 46–56.

Holland, T.J.B., 1983. The experimental determination of activities in disordered and short-range ordered jadeitic pyroxene. Contributions to Mineralogy and Petrology 116, 433–447.

Holland, T.J.B., Blundy, J., 1994. Non-ideal interactions in calcic amphiboles and their bearing on amphibole-plagioclase thermometry. Contributions to Mineralogy and Petrology 82, 214–220.

Jahn, B.M., Caby, R., Monié, P., 2001. The oldest UHP eclogites of the world: age of UHP metamorphism, nature of protoliths and tectonic implications. Chemical Geology 178, 143–158.

Kilian, C., 1932. Sur les conglomérats précambriens du Sahara central: le Pharusien et le Suggarien. Comptes Rendus de l'Académie des Sciences Paris 7, 87.

Lachenbruch, A.H., Sass, J.H., Galanis Jr., S.P., 1985. Heat flow in southernmost California and the origin of the Salton trough. Journal of Geophysical Research 90, 6709–6736.

Latouche, L., 1975. Structure et formation des couloirs plissés panafricains dans la région des Gour Oumelalen (Nord-Est de l'Ahaggar, Algérie). Bulletin de la Société Géologique de France 7, 594–603.

Latouche, L., 1978. Etude pétrographique et structurale du Précambrien de la région des Gour Oumelalen (Nord-Est de l'Ahaggar, Algérie). Thèse d'Etat, 255 p.

Latouche, L., 1983. L'orthoferrosilite et les roches associées de la région des Gour Oumelalen (Nord-Est de l'Ahaggar, Algérie). Bulletin de Minéralogie 106, 329–339.

Latouche, L., 1985. Les collisions intracratoniques et la tectonique tangentielle dans le Pan-Africain du Hoggar central. In: Evolution géologique de l'Afrique. Publication occasionnelle CIFEG 4, pp. 143–158.

Latouche, L., Vidal, P., 1974. Géochronologie du Précambrien de la région des Gour Oumelalen (Nord-Est de l'Ahaggar, Algérie). Un exemple de mobilisation du strontium radiogénique. Bulletin de la Société Géologique de France 16, 195–203.

Leloup, P.H., Kienast, J.R., 1993. High temperature metamorphism in a major strike-slip shear zone: the Ailao Shan–Red River, People's Republic of China. Earth and Planetary Science Letters 118, 213–234.

Lelubre, M., 1952. Recherche sur la géologie de l'Ahaggar central et occidental (Sahara central). Bulletin Service géologique Algérie, 22, tome 1, 354 p, tome 2, 387 p.

Liégeois, J.-P., Black, R., 1987.Alkaline magmatism subsequent to collision in the Pan-African belt of the Adrar des Iforas. In: Fitton, J.G., Upton, B.G.J. (Eds.), Alkaline Igneous Rocks. The Geological Society, Blackwell Scientific Publication 30, pp. 381–401.

Liégeois, J.P., Bertrand, J.M., Black, R., 1987. The subduction- and collision-related Pan-African composite batholith of the Adrar des Iforas (Mali): a review. In: Kinnaird, J., Bowden, P. (Eds.), African Geology Review. John Wiley, London, pp. 185–211. and Geological Journal 22, 185–211.

Liégeois, J.P., Black, R., Navez, J., Latouche, L., 1994. Early and late Pan-African orogenies in the Aïr assembly of terranes (Tuareg shield, Niger). Precambrian Research 67, 59–88.

Liégeois, J.P., Diombana, D., Black, R., 1996. The Tessalit ring complex (Adrar des Iforas, Malian Tuareg shield): a Pan-African, post-collisional, syn-shear, alkaline granite intrusion. In: Demaiffe, D. (Ed.), Petrology and Geochemistry of Magmatic Suite of Rocks in the Continental and Oceanic Crusts. ULB-MRAC, Bruxelles, pp. 227–244.

Liégeois, J.P., Navez, J., Hertogen, J., Black, R., 1998. Contrasting origin of post-collisional high-K calc-alkaline and shoshonitic versus alkaline and peralkaline granitoids. Lithos 45, 1–28.

Ludwig, K.R., 1999. Using Isoplot/Ex Version 2.01, A Geochronological Toolkit for Microsoft Excel. Berkeley Geochronology Center Special Publication 1a, 47 p.

Lugmair, G.W., Marti, K., 1978. Lunar initial $^{143}Nd/^{144}Nd$: differential evolution of the lunar crust and mantle. Earth and Planetary Science Letters 39, 349–357.

Martin, H., 1987. Archaean and modern granitoids as indicators of changes in geodynamic processes. Revista Brasiliensis de Geosciencias 17, 360–365.

Maxson, J., Tikoff, B., 1996. Hit-and-run collision model for the Laramide orogeny, western United States. Geology 24, 968–972.

Mouri, H., Guiraud, M., Hensen, B.J., 1996. Petrology of sapphirine-bearing Al–Mg granulites from Ihouhaouene, In Ouzzal, Hoggar, Algeria: an example of phlogopite stability at high temperature. Journal of Metamorphic Geology 14, 725–738.

Navez, J., 1983. Détermination de 11 éléments en traces dans les roches silicatées par spectrométrie d'émission dans un plasma à couplage inductif. Rapport Annuel du Département de Géologie et Minéralogie 1981–1982 Musée Royal de l'Afrique Centrale, Tervuren, Belgique, pp. 115–118.

Navez, J., 1995. Détermination d'éléments en traces dans les roches silicatées par ICP-MS. Rapport Annuel du Département de Géologie et Minéralogie 1993–1994 Musée Royal de l'Afrique Centrale, Tervuren, Belgique, pp. 139–147.

Navez, J., Liégeois, J.P., Latouche, L., Black, R., 1999. The Palaeoproterozoic Tchilit exotic terrane (Aïr, Niger) within the Pan-African collage of the Tuareg shield. Journal of Geological Society London 156, 247–259.

Nelson, B.K., DePaolo, D.J., 1985. Rapid production of continental crust 1.7 to 1.9 b.y. ago: Nd isotopic evidence from the basement of the North Americam midcontinent. Geological Society of America Bulletin 96, 746–754.

Norrish, K., Hutton, J.T., 1969. An accurate X-ray spectrographic method for the analysis of a wide range of geological samples. Geochimica et Cosmochimica Acta 33, 431–453.

Ouzegane, K., Boumaza, S., 1996. An example of ultrahigh-temperature metamorphism: orthopyroxene-sillimanite-garnet, sapphirine-quartz parageneses in Al–Mg granulites from In Hihaou, In Ouzzal, Hoggar. Journal of Metamorphic Geology 14, 693–708.

Paquette, J.L., Caby, R., Djouadi, M.T., Bouchez, J.L., 1998. U–Pb dating of the end of the Pan-African orogeny in theTuareg shield: the post-collisional syn-shear Tioueine pluton (Western Hoggar, Algeria). Lithos 45, 245–254.

Peacock, S.M., 1993. The importance of blueschist ⇒ eclogite dehydration reactions in subduction oceanic crust. Geological Society of America Bulletin 105, 684–694.

Pearce, J., 1982. Role of the sub-continental lithosphere in magma genesis at active continental margins. In: Hawkesworth, C.J., Norry, M.J. (Eds.), Continental Basalts and Mantle Xenoliths. In: Shiva Geology Series, Nantwich, pp. 230–249.

Peucat, J.J., Drareni, A., Latouche, L., Deloule, E., Vidal, P., 2003. U–Pb zircon (TIMS and SIMS) and Sm–Nd whole-rock geochronology of the Gour Oumelalen granulitic basement, Hoggar massif, Tuareg shield, Algeria. Journal of African Earth Science, this issue.

Pineau, F., Latouche, L., Javoy, M., 1976. L'origine du graphite et les fractionnements isotopiques du carbone dans les marbres métamorphiques des Gour Oumelalen (Ahaggar, Algérie), des Adirondacks (New Jersey, USA), et du Damara (Namibie, Sud-Ouest Africain). Bulletin de la Société Géologique de France 7, 1713–1723.

Powell, R., Holland, T.J.B., 1988. An internally consistent thermodynamic dataset with uncertainties and correlations: 3. Application methods, worked examples and a computer program. Journal of Metamorphic Geology 6, 173–204.

Sautter, V., 1986. Les éclogites de l'Aleksod (sud algérien): des témoins in situ d'une collision intracontinentale. Journal of African Earth Science 5, 345–357.

Spear, F.S., 1993. Metamorphic Phases Equilibria and Pressure–Temperature–Time Paths. Mineralogical Society America, BookCrafters, Inc, MI, USA. 799 p.

Steiger, R.H., Jäger, E., 1977. Subcommission on geochronology: convention on the use of decay constants in geo- and cosmochronology. Earth and Planetary Sciences Letters 36, 359–362.

Streckeisen, A., Le Maitre, R.W., 1979. A chemical approximation to the modal QAPF classification of the igneous rocks. Neues Jahrbuch fur Mineralogie Abteilung 136, 169–206.

Sun, S.S., 1980. Lead isotopic study of young volcanic rocks from mid-ocean ridges, ocean islands and islands arcs. Philosophical Transactions of the Royal Society of London A 297, 409–445.

Taylor, S.R., Mc Lennan, S.M., 1985. The Continental Crust: Its Composition and Evolution. Blakwell, Oxford. 312 p.

Williams, M.L., Grambling, J.A., 1991. Manganese, ferric iron, and the equilibrium between garnet and biotite. American Mineralogist 75, 886–908.